Montanuniversität Leoben

Sputter Deposition of Amorphous Carbon Thin Films in Argon, Neon and Helium Atmospheres

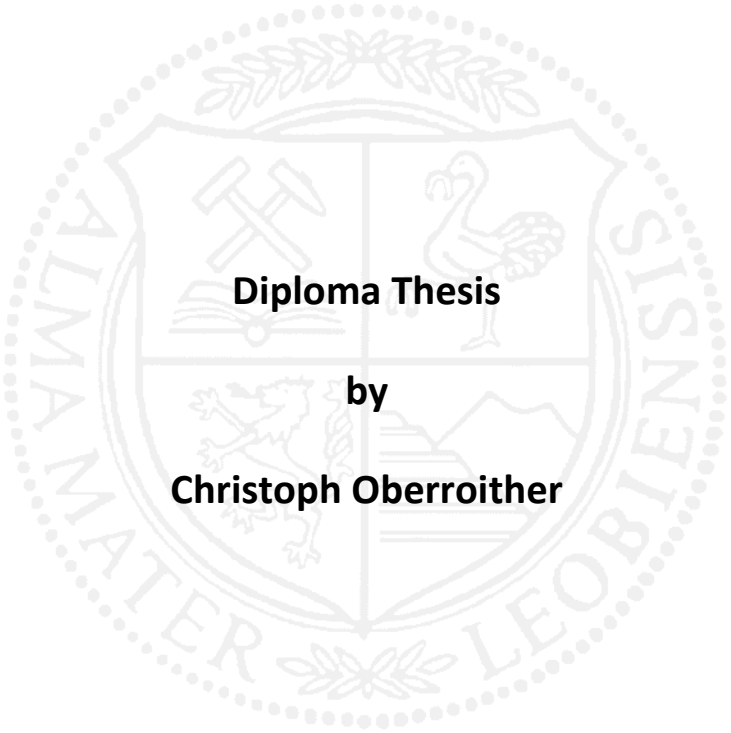

Diploma Thesis

by

Christoph Oberroither

This work has been carried out at the Chair of Functional Materials and Material Systems, Montanuniversität Leoben, Austria

Leoben, June 2017

This work was financially supported by the Austrian Federal Government (in particular from Bundesministerium für Verkehr, Innovation und Technologie and Bundesministerium für Wissenschaft, Forschung und Wirtschaft) represented by the Österreichische Forschungsförderungsgesellschaft mbH within the project SmartCoat-Eco (project number 843621).

Affidavit

I declare in lieu of oath, that I wrote this thesis and performed the associated research myself, using only literature cited in this volume.

Leoben, June 2017

Acknowledgments

I want to express my sincere gratitude to Univ. Prof. DI Dr.mont. Christian Mitterer, head of the Chair of Functional Materials and Material Systems, for the opportunity to write this interesting thesis and for his professional supervision.

I am very grateful to my supervisor DI Christian Saringer, for all his valuable advice from the beginning and his seemingly never ending patience. His scientific knowledge, quick responses to my questions and precise corrections were more than helpful for the completion of this thesis.

Furthermore, I would like to thank all members of the Thin Film Group for their help and great support whenever it was needed and the pleasant work atmosphere.

Some special thanks go to all my friends I found during my time in Leoben. The mutual motivation to study and their helpfulness in every situation is what made my studies in this town so special.

Last but not least, I want to thank my entire family, especially my parents for their financial support and endless encouragement through the years. Without them, it would not have been possible for me to complete my studies.

Table of Contents

Page

1 Introduction

Amorphous carbon (a-C) is considered to be a versatile material, serving as a protective coating for numerous optical and tribological applications [1–6]. The attractive properties of a-C include high mechanical hardness [7], good wear resistance [8], chemical inertness [9], high thermal and low electrical conductivity [7,10]. Due to this broad spectrum of properties, they often serve as coatings in areas such as optical windows, magnetic storage disks, cutting tools, biomedical instruments, electromechanical devices and in the automobile industry [1–6].

Different types of a-C coatings can be grown by using a variety of deposition techniques such as electron beam evaporation [11], magnetron sputtering [10], carbon ion beam deposition [12], cathodic arc evaporation [13] and plasma enhanced chemical vapour deposition [14]. Depending on the deposition method, the structure of a-C films can range from diamond like to graphite like. One of the most widely used methods of depositing a-C films is magnetron sputtering. It is usually performed in Ar atmosphere and with a graphite target. It is commonly used for industrial applications because of its versatility and its scalability in size. The disadvantage of magnetron sputtering, however, is the difficulty to produce coatings with diamond like character, i.e. mainly high hardness, due to the relatively low particle energies present in the plasma [1].

In order to be able to obtain films with precisely adjusted properties, it is necessary to investigate their dependence on the deposition parameters. It has been demonstrated in numerous studies that the properties of a-C coatings deposited by magnetron sputtering are mainly governed by the energy of the carbon particles during deposition and the substrate temperature [1,10,15–17]. However, open questions on how the discharge power influences the process and coating properties remain.

Therefore, the aim of this thesis was to investigate the properties of a-C films influenced by the power density and bias voltage during the sputter deposition process. a-C coatings were synthesized at different power densities in Ar, Ne and He. Furthermore, the bias potential was varied to determine the influence of the particle energy on microstructure and properties of those coatings deposited in Ar. The microstructure and the chemical composition were investigated by X-ray diffraction, Raman spectroscopy and elastic recoil detection analysis. Electrical and mechanical properties of the films where determined by resistivity measurements, wafer curvature measurements and nanoindentation.

2 Theoretical background

2.1 Bonding types of carbon

The chemical element carbon has the outstanding ability of being able to bond with itself and other elements in various ways. Therefore, it exhibits a variety of different structures with diverse properties in its solid state which also makes it the base element for organic chemistry [2].

The electronic configuration of the carbon atom in its state of lowest energy is $1s^2 2s^2 2p^2$. It is a tetravalent element which is able to form three different hybrid bonds, i.e. the sp^3, sp^2 and sp^1 bond, as seen in Fig. 2.1. The enthalpy of carbon-carbon bonds increases from the single to the triple bond, the length of which strongly depends on the molecular environment [1].

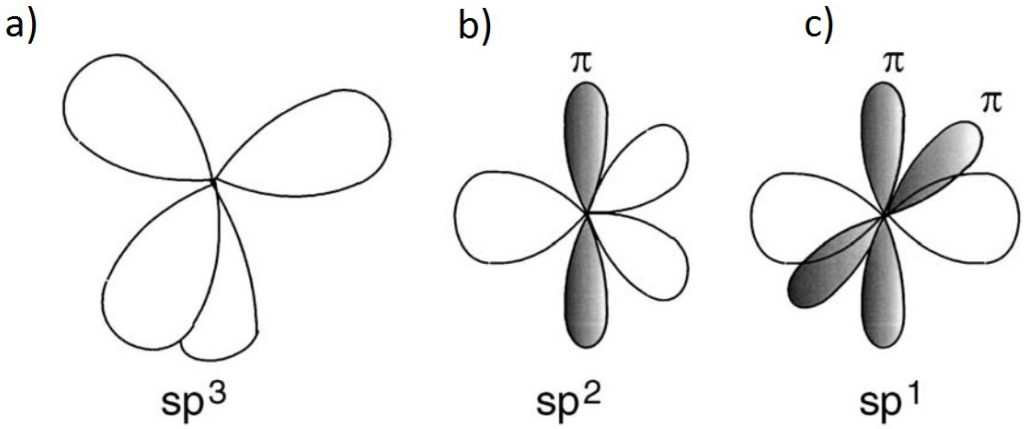

Figure 2.1: Schematic presentation of the sp^3 (a), sp^2 (b) and sp^1 (c) bonding states occurring in carbon [2].

2.1.1 Diamond like bonding

Diamond is one of the crystalline forms of carbon. In the cubic form of diamond, each carbon atom is connected to four other carbon atoms through covalent bonds, where all bonds are in the sp^3 configuration (Fig. 2.1 (a)). These four σ orbitals form the strongest type of carbon bonds and are arranged in tetrahedral configuration with bond angles of 109.5°. Due to this strong type of bonding, diamond has unique physical properties. Diamond possesses the largest bulk modulus, the highest density, the largest thermal conductivity at room temperature and the smallest thermal expansion coefficient of all solid materials. Furthermore, it is a wide band gap semiconductor with a band gap of 5.5 eV with the largest limiting hole and electron velocities [1]. Due to its high dispersion of light, diamond is frequently used as a gemstone. In industrial applications diamond is used as a polishing, grinding and cutting material because of its high hardness and thermal conductivity [3].

2.1.2 Graphite like bonding

The basis for the crystal structure of graphite is the graphene or carbon layer. In graphite, these layers are stacked in an ABABAB sequence. Each layer consists of a hexagonal array of covalently bonded carbon atoms in sp^2 configuration (Fig. 2.1 (b)). In this configuration three σ orbitals with bond angles of 120° in-plane and a π orbital perpendicular to the plane are formed. This π orbital forms a by far weaker bonding with the same orbitals of neighbouring planes. This weak interlayer bonding is the reason that the graphite planes are able to easily move relatively to each other when they are exposed to shear forces. This type of bonding therefore makes the graphite a good electric conductor and an effective solid lubricant [1,2].

2.1.3 Chain like bonding

In the sp^1 hybridisation of carbon (Fig. 2.1 (c)) two of the four valence electrons of the carbon atom form a σ bond, being aligned along the bond-axis. The remaining two valence electrons are excited into π orbitals which are directed normal to the bond axis. In contrast to sp^3 and sp^2 bonds, which can form three and two dimensional structures, sp^1 bonds are only one dimensional. This results in a chain-like shape which mainly occurs in organic molecules (e.g. hydrocarbon acetylene) and is of lesser importance in solid carbon-based materials [2].

2.1.4 Carbon nanotubes and fullerenes

Two further mentionable allotropes of carbon are carbon nanotubes and fullerenes. The basic component of these allotropes is the graphene sheet, which is a two-dimensional layer of graphite. The atoms are densely packed in a regular hexagonal pattern and in a sp^2 hybridization. Nanotubes can be seen as rolled up graphene sheets. They can reach relatively long lengths up to several micrometres while the diameter is very small, down to 0.7 nanometres. Fullerenes are hollow carbon molecules which exist in a variety of shapes and sizes. One of the most stable fullerene molecules is the C_{60} molecule, commonly known as Buckminster-fullerene. It consists of 12 pentagons and 20 hexagons and shows a similar bonding behaviour as graphene. These forms of carbon allotropes show unique mechanical and electrical properties making them promising materials for future fields of application [2,18].

2.2 Amorphous carbon

In contrast to diamond and graphite, amorphous carbon (a-C) does not possess a clearly defined crystal structure. As typical for an amorphous material, the atoms in a-C only have a short-range order and the type of bonding is a mixture of both, graphite like sp^2 and diamond like sp^3 bonds. The most important parameter defining the order and hence the type of the a-C is the relative amount of each bonding type [19]. Furthermore, an important factor is the order of the sp^2 bonds, which has a significant influence on the electronic properties of carbon.

In order to modify the structure and properties of the material considerably, hydrogen (H) is often introduced to the carbon-based material [19]. Jacob and Moller [20] and Ferrari and Robertson [21] have developed a ternary phase diagram to display the different varieties of a-C types, depending on of the hydrogen content and the sp^2/sp^3 phase fraction, see Fig. 2.2 [20,21].

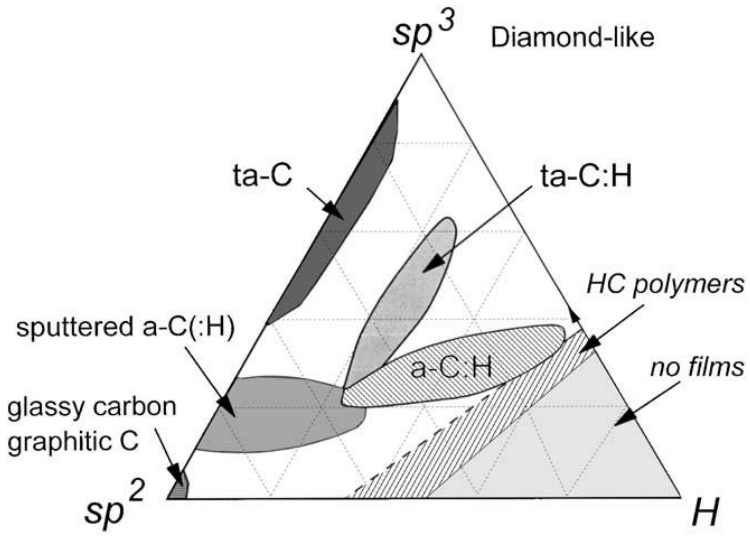

Figure 2.2: Ternary phase diagram showing the different types of a-C coatings as a function of the sp^2, sp^3 and H content [1].

The variation of the sp^3 content in a-C can range from 5 % to 85 % [1,13]. The a-C coatings featuring the lowest amount of sp^3 bonds are located in the lower left hand corner of the diagram. To deposit such a-C coatings, electron beam evaporation and magnetron sputtering are used. These coatings have only a small number of sp^3 clusters formed by a few atoms and hardly any H content. Therefore, they exhibit mainly graphitic properties. When a-C contains predominately an sp^3 bond network, it is usually termed tetragonal amorphous carbon (ta-C) [11]. Such structures share comparable properties to diamond, including the high hardness and elastic modulus, the wide band gap and the electrochemical and chemical inertness [1]. ta-C thin films are deposited by carbon ion beam deposition or by cathodic arc evaporation

[10]. The materials hydrogenated amorphous carbon (a-C:H) and the less H containing tetrahedral hydrogenated amorphous carbon (ta-C:H), are located in the central region of the ternary system and show a reasonably even distribution of the three components. In general, it can be said that H rich a-C films are softer and have less internal stresses than H free films [6]. They are deposited by plasma enhanced chemical vapour deposition [1]. When the H content is increased, hydrocarbon films like polyethylene or polyacetylene, for instance, are produced. The phase diagram also shows, that there is a limit for the H that can be added to obtain a solid film. Above this limit only volatile molecules are formed and no solid films can be produced. Table 1 shows the discussed variation of properties for the different forms of a-C coatings in comparison with diamond and graphite [1].

Table 1: Property variation of a-C materials in comparison with diamond and graphite.

	sp^3 content [%]	**density [g/cm³]**	**band gap [eV]**	**hardness [GPa]**	**elastic modulus [GPa]**	**reference**
diamond	100	3.515	55	100	1000	[1,3]
graphite	0	2.267	0	2.25	27	[1,4]
a-C	5	2.2	0.5	11-22	110-180	[1,22]
ta-C	80-88	3.1	2.5	80	490-757	[1,22]
a-C:H	40-60	1.2-2.2	1.1-4	10-20	146-148	[1,22]
ta-C:H	70	2.4	2-2.5	50	300	[1,22]

2.3 Sputter deposition

Sputter deposition belongs to the comprehensive group of physical vapour deposition (PVD) techniques. Characteristic for PVD methods is, that the material for subsequent film deposition is transferred to the vapour by physical processes, usually from a solid source. The material is broken up into molecules and atoms to be subsequently transported through a vacuum or plasma environment. The vapour then condenses on surfaces where a thin film is formed. The film thickness can vary from a few nanometres up to a several micrometres and coatings can be deposited onto different substrates with dimensions reaching from few millimetres for semiconductor materials up to large planes being used for architectural purposes [23].

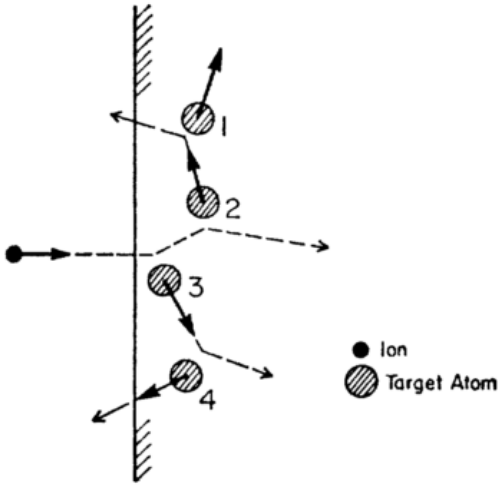

Figure 2.3: Schematic of a collision cascade leading to the sputtering of atoms [24].

During sputter deposition, the material that is to be deposited is vaporized by a momentum transfer from accelerated ions to the atoms of the so-called target [23]. The ions which impact on the target surface, cause collision cascades displayed in Fig. 2.3, which lead to the ejection of atoms. Atoms can only be vaporized when they receive a momentum perpendicular to the target surface outwards (atom 2 and 4). If their thus gathered energy is larger than the surface binding energy the atoms leave the target, are transported to the substrate surface, condensate and consequently form a film. The ions taking part in the sputtering process are supplied by either an ion gun or an electric discharge [23]. The number of particles ejected from the target surface is described by the so-called sputter yield, which is defined as the average target atoms being emitted per impacting Ion. Under vertical ion bombardment, the sputtering yield shows an increase with energy until it reaches its maximum at several 10^4 eV. A continued increase of energy leads to a decrease of the yield due to a more pronounced ion implantation. The sputter-yield is furthermore dependent on the target material as well as the

mass of the impacting Ions. The energy transfer is maximal, when the mass of the ions is the same as the mass of the target atoms [24–26].

2.3.1 Magnetron sputtering

Conventional diode sputtering has various advantages compared to other techniques, however, it is known to have low deposition rates, a low ionisation efficiency in the discharge and to possess pronounced substrate heating effects [1,27]. Owing to the long electron mean free path, the substrate is heated but the ions that are required for sputtering are not produced. The solution to these problems is the combination of the diode sputtering process with a magnetic field: To enhance the ionisation efficiency, magnets are placed behind the target. The magnetic field lines thus created are configured parallel to the target surface confining the electrons close to the target region, forcing them to gyrate which increases their path length. Hence the degree of ionisation above the target rises, resulting in higher sputtering rates and consequently higher deposition rates. The improvement of the ionisation allows the sputtering process to be run under lower chamber pressures. As a result, the probability of colliding target atoms within the gas is reduced, further increasing the deposition rate [1,28].

Depending on the magnetic configuration, magnetron sputtering can be categorized into two different types:

- conventional balanced magnetron sputtering
- unbalanced magnetron sputtering

The different arrangements of the magnetic field are illustrated in Fig. 2.4. In conventional balanced magnetron sputtering, which is shown in Fig. 2.4(a), the field lines are closed and loop over the target surface because the inner and outer magnets possess a similar strength [29]. In unbalanced magnetron sputtering the strength of the inner and outer poles differ from each other. There are two types of the unbalanced magnetron: In type-1, which is shown in Fig. 2.4(b), the outer pole is weakened in relation to the inner pole. If this is the case, the plasma density near the substrate is low because the field lines which are not closed get directed towards the deposition chamber walls. This is a rather undesirable state in which the ion currents have a low value close to the substrate. It sometimes is purposely used to produce coatings with controlled porosity in the order of 1000 times greater than in fully dense materials, making them suitable as catalyst materials [27]. In type-2, presented in Fig. 2.4(c), some of the field lines are closed while others lead up to the substrate. These field lines enable secondary electrons emitted at the target to follow the field lines to the substrate surface and ionise atoms on their way. Therefore, the plasma is no longer restricted to the near target

area and stretches to the substrate [27]. This extended plasma leads to the ionisation of atoms that can reach the substrate, resulting in improved coating properties such as hardness and density [29].

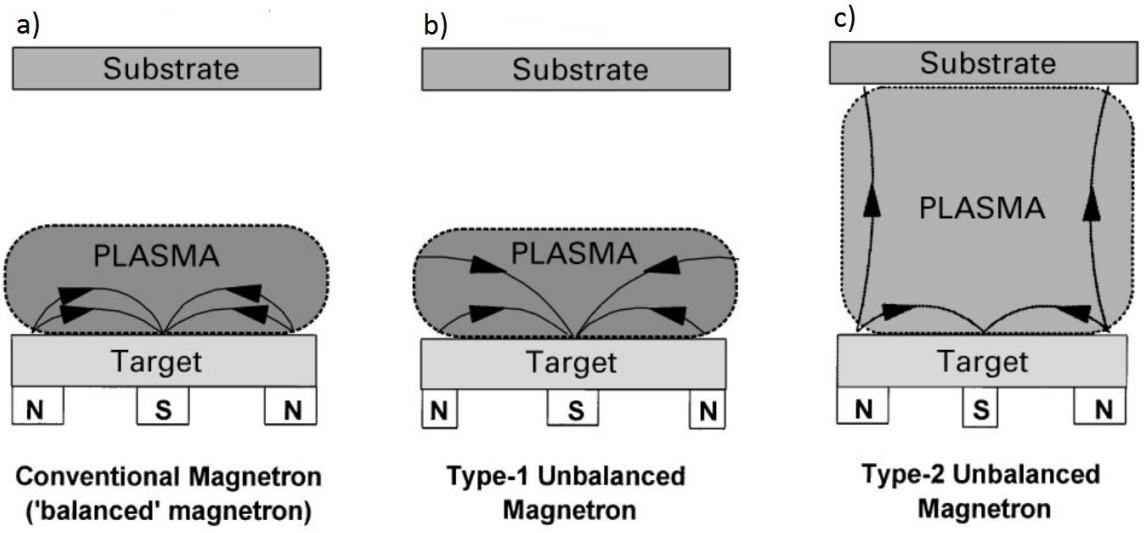

Figure 2.4: Schematic representation of the three different plasma configurations: a) balanced magnetron b) type-1 unbalanced magnetron and c) type-2 unbalanced magnetron [27].

2.3.2 Bias-sputtering

Generally, conventional diode sputtering holds the substrate retainers on mass potential. Usually, however, a bias voltage is applied to the substrate holder during sputter deposition, mainly in the range from -50 to -100 V. The substrates are then on a negative potential compared to the plasma and therefore they are exposed to constant ion-bombardment during the deposition process. In general, it can be argued, that an applied bias potential to the substrate leads to films with a higher density and improved structural properties. Furthermore, the constant ion bombardment removes loosely adsorbed impurities on the steady growing thin film [26]. Thus, bias sputtering can improve the purity of the films [30].

2.3.3 Sputter deposition of a-C

Unbalanced magnetron sputtering is a method that is commonly used for the deposition of a-C thin films, using graphite as a target material. The fraction of sp^2 and sp^3 bonds in the coating is influenced by the energy of the impacting particles [1]. Figure 2.5 shows that the sp^3 fraction is related to the ion energy. The sp^2 phase dominates up to an energy of about 30 eV [31]. After that the curve continuously rises at a high gradient until it reaches its maximum of about 80 % sp^3. This peak is obtained at an energy of 100 eV were the carbon is deposited in the form of ta-C [32,33]. A further increase in energy does not lead to a higher fraction of

diamond like sp^3 bonding, but favours a graphite like bonding instead. This effect occurs because not all of the energy is used to displace atoms, but is increasingly converted into heat which fosters a graphitization and therefore the generation of sp^2 bonds [34]. The magnetron sputtering process typically operates at low ion energy levels and the thin films are composed of a-C, with only a low amount of sp^3 bonds.

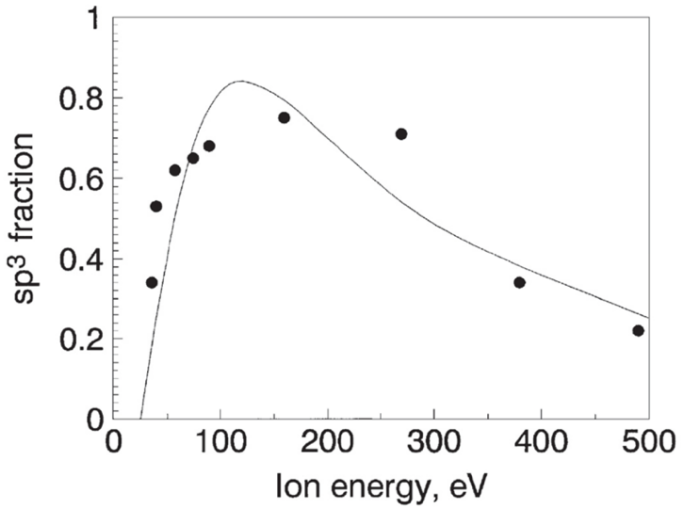

Figure 2.5: Diagram showing the ion energy dependency of the sp^3 phase fraction [31].

Figure 2.6 shows the influence of the deposition temperature on the sp^3 fraction of coatings obtained at an ion energy of 90 eV. The diagram demonstrates that at deposition temperatures below 150 °C the fraction of sp^3 bonds is constantly at values exceeding 80 % When the deposition temperature exceeds 150 °C, however, the sp^3 fraction rapidly drops. This sharp fall occurs at the so called transition temperature which marks the transformation from ta-C to a-C [35]. When the sp^2 phase becomes predominant, the density of the thin film decreases while the deposition rate increases [35].

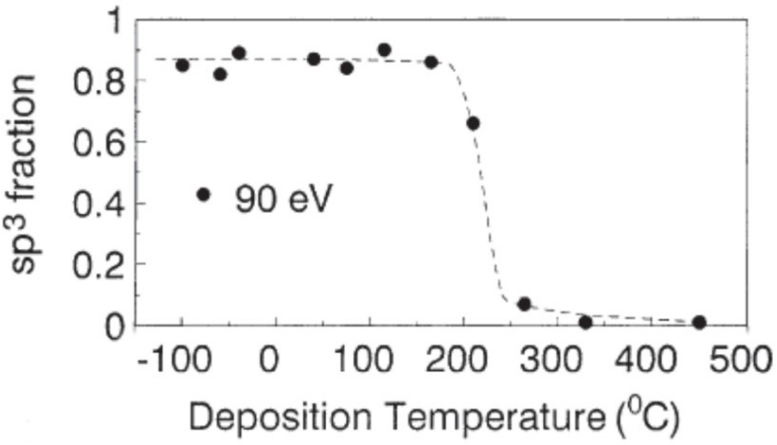

Figure 2.6: Diagram of the sp^3 bond fraction as a function of the deposition temperature [35].

Figure 2.5 and Fig. 2.6 demonstrate that a high sp^3 content can only be achieved at particle energy levels between 50 and 100 eV and at substrate temperatures below 150 °C.

As previously discussed, the ion energy has a great impact on the sp^3 content and consequently on the mechanical properties of the film. The ion energy is greatly influenced by deposition pressure. At high pressures the mean free path of the atoms decreases, elevating the probability of collisions with other atoms. These collisions reduce the energy of the atom and only a small fraction of atoms is able to transfer enough energy to the substrate surface, to induce sp^3 bonding in the film. At low pressures the atoms can reach higher energy levels, which results in more energetic ion bombardment and consequently in films with a high sp^3 bonding concentration. Due to this high energy and high fraction of sp^3 bonding, the hardness and the internal stresses in the film increase. Figure 2.7 shows the development of hardness with increasing deposition pressure [36].

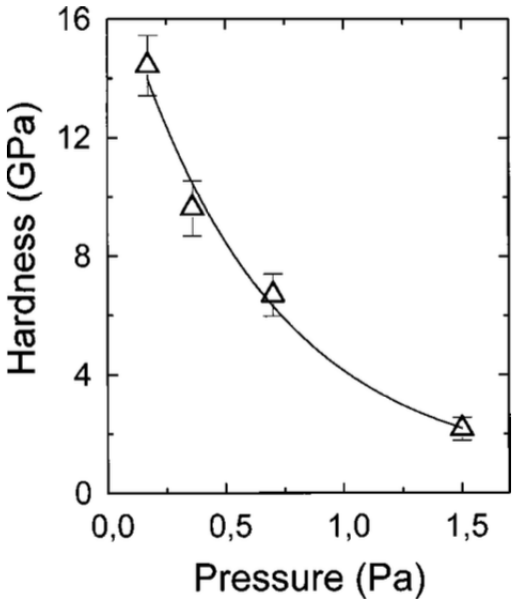

Figure 2.7: Diagram of the hardness of a-C films as a function of the deposition pressure [36].

2.4 Thin film growth

The basic interactions between substrate surfaces and arriving particles are illustrated in Fig. 2.8. After condensation from the vapour phase, particles can generally behave in two different ways:

- immediately re-evaporate
- diffuse along the surface.

If the particles re-evaporate, which mainly occurs at sufficiently high temperatures, they are lost for film growth. The diffusing particles, on the other hand, can either be adsorbed, especially at sites like edges and defects, or re-evaporate after a certain time. Besides the adsorption and surface diffusion, nucleation of several particles and film growth can occur, which results in the formation of a film. Another process that may occur during film growth is the exchange of atoms between the film and substrate. This is termed interdiffusion and is an important process to smoothen the film-substrate interface. The structure of the condensed film material is influenced by the mass of the particles, the vapour pressure and the source temperature [37].

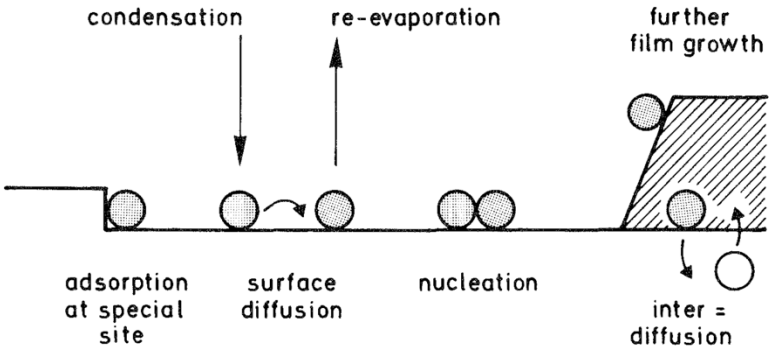

Figure 2.8: Schematic representation of interactions between surfaces and particles condensing from the vapour [37].

Generally, three different modes of film growth can be distinguished. The first is the layer by layer growth as seen in Fig. 2.9(a). In this mode, the interaction between the layer atoms and the substrate atoms are stronger than between neighbouring layer atoms. Therefore, a new layer only starts to form after the former one is completed. The second mode is named island growth and is shown in Fig. 2.9(c). An island is a multilayer conglomerate of adsorbed atoms. In this mode, the interactions between neighbouring atoms are stronger than between substrate and film atoms. The third mode is called layer plus island mode and is represented in Fig. 2.9(b). After the formation of one to several monolayers, island growth occurs on top of them. This is an intermediate case and is a combination of both, the layer by layer and the island growth. Lattice mismatches occurring at the interface between the deposited film and the substrate cannot be sustained into the bulk of the film. Hence, monolayers cannot continue to form and island growth tends to exist [37].

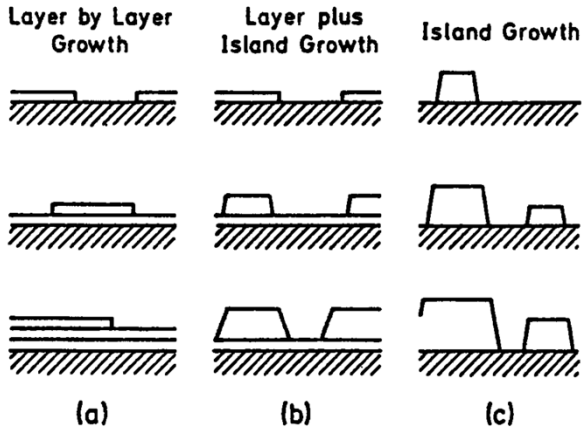

Figure 2.9: Schematic representation of the three film growth modes: (a) layer by layer growth, (b) layer plus island growth and (c) island growth [37].

2.5 Raman spectroscopy

2.5.1 The Raman effect

Raman spectroscopy is a non-destructive method that is often used to estimate phase compositions, bonding types, the degree of crystallinity and internal stresses of materials [38]. The Raman effect, which is the inelastic scattering of photons with molecules and phonons, was discovered by C. V. Raman and K. S. Krishnan in liquids and independently verified in crystals by G. and L. Mandelstam [39]. When a photon interacts with a molecule or phonon, it is most likely that an elastic scattering process occurs. If the photon scatters elastically, its energy and consequently the wavelength is not changed during the scattering process. However, in some cases it happens that the photon scatters inelastically, which results in a change of the vibrational state of the material. This inelastic scattering process is termed Raman scattering. The energy difference between the two mentioned states, leads to a change of the wavelength of the photons, which is called the Raman-shift. There are two types of Raman-shifts [40]:

- Stokes-Raman-scattering: Energy is transferred from the incident photon to the material creating a phonon or elevating the molecule to a higher vibrational state, which shifts the wavelength of the photon to higher values.

- Anti-Stokes-Raman-scattering: The incident photon absorbs the energy of a phonon or vibration present in the material and energy is transferred from the scattering material to the scattered photon, resulting in a shift of the wavelength to lower values. At ambient temperature, most molecules are in their vibrational ground state and only a very small percentage are in the vibrational exited state [38]. Therefore, this effect is minor when compared to the Stokes-Raman-scattering.

The shifted wavelength is detected by a spectrometer. The photons which are admitted onto the investigated material typically originate from a monochromatic light source, such as lasers whose wavelengths can range from the infrared to near ultraviolet region.

2.5.2 Raman spectroscopy of a-C

Raman spectroscopy enables the investigation of the different bonding types present in carbon and the bonding behaviour of a-C. Typical Raman-spectra of carbon based materials are shown for comparison in Fig. 2.10 [1].

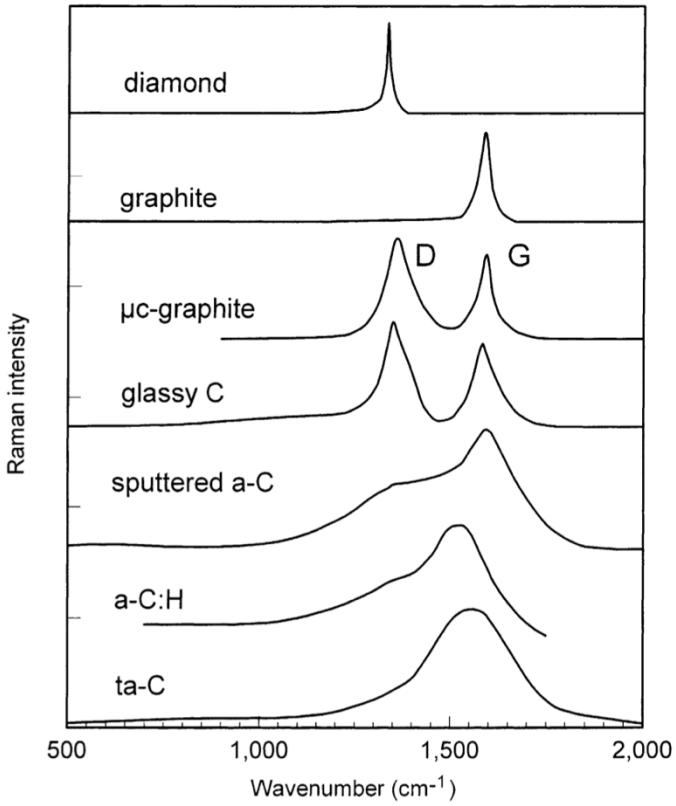

Figure 2.10: Comparison of Raman spectra for the different types of carbon based materials [1].

Diamond and single crystalline graphite each have a single Raman active mode at 1332 cm^1 and 1580 cm^{-1}, respectively. When the graphite is disordered, as it is typical for sputtered a-C materials, a second mode around 1350 cm^{-1} appears. These modes are termed G-mode and D-mode. The G-mode is the in-plane-bond-stretching of any pair of sp^2 bonded carbon atoms. Its vector-form is shown in Fig. 2.11 (a). The G-mode is seen in all sp^2 sites including carbon chains and not only in aromatic rings. The D-mode is the breathing mode of those sp^2 sites occurring in rings bonds but is never seen in chain like bonding. Its vector-form is shown in Fig. 2.11(b) [21].

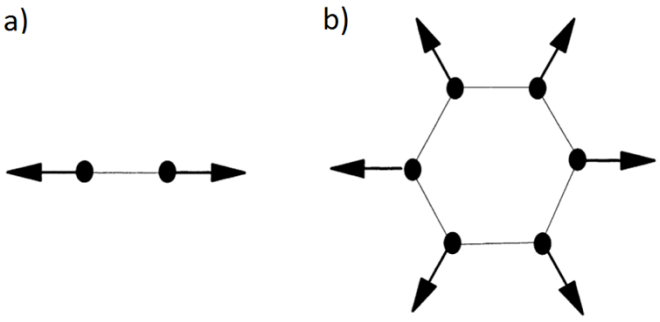

Figure 2.11: Vector-form of the a) G and b) D-mode of a-C [1].

To investigate the ratio of sp^2 and sp^3 bonds, it is necessary to differentiate these two different modes of graphite. A practical way of doing that is the determination of the intensity ratio of the D-peak (I(D)) and the intensity of the G-peak (I(G)). The I(D)/I(G) intensity ratio is inversely proportional to the grain size or the in-plane correlation length L_a of the graphite [41]

$$\frac{I(D)}{I(G)} = \frac{c}{L_a} . \tag{1}$$

Here, c stands for the Raman coupling coefficient. This implies that I(D)/I(G) is proportional to the number of rings at the edge of the graphite's grains. This, in combination with the location of the G-peak position, is the most common way to classify a-C materials. The procedure can be used to qualitatively determine the sp^3 content in the material [1].

The Raman spectrum of a-C materials is influenced by the clustering of the sp^2 phase, their bond disorder, the presence of sp^2 rings and the ratio of sp^2 and sp^3 phase content [21]. Figure 2.12 illustrates a typical Raman measurement of a-C and in which way the intensity and the positions of the D and G peaks are influenced by the coating microstructure.

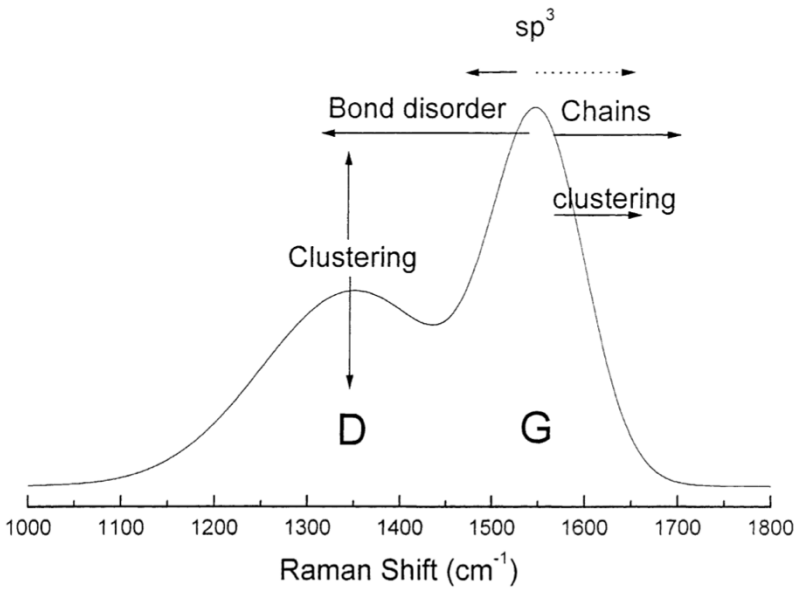

Figure 2.12: Schematic illustration of a Raman measurement of a-C with factors influencing the location and intensity of the G and D peaks [1].

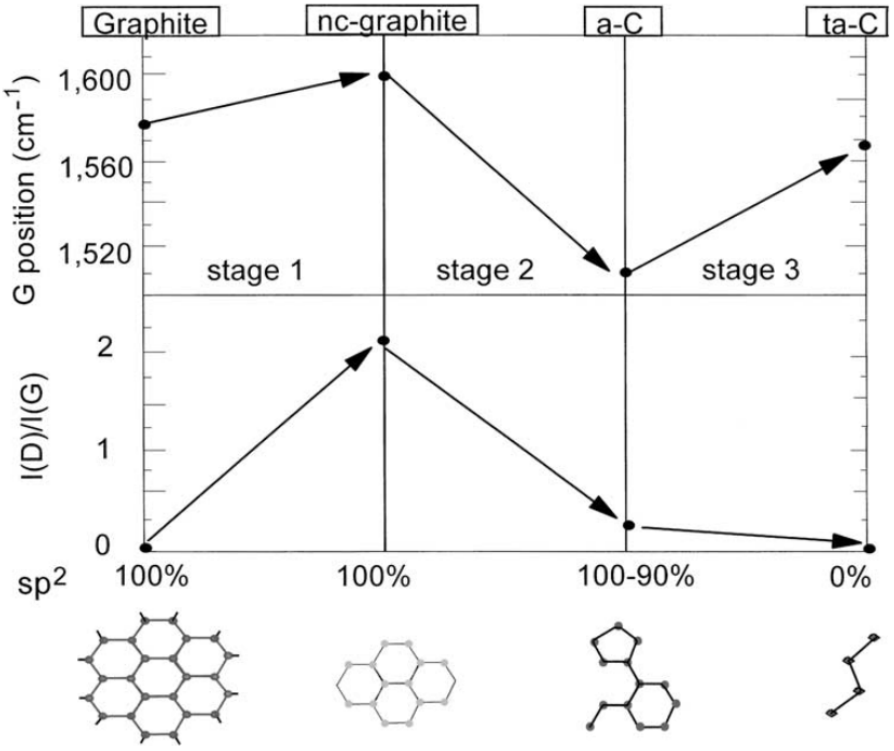

Figure 2.13: Variation of the G-peak wavenumber and the I(D)/I(G) ratio with increasing degree of disorder of the carbon [1].

On the basis of the G-band position and the I(D)/I(G) ratio, Ferrari and Robertson [21] divided the Raman-spectra of carbons by their growing degree of disorder into three stages (Fig. 2.13).

• **Stage 1:** from graphite to nano-crystalline graphite: The main effects on the Raman-spectra in this stage are a shift of the G-peak from 1580 to 1600 cm^{-1} and the appearance of the D-peak. Therefore, the I(D)/I(G) ratio increases [21].

• **Stage 2:** from nano-crystalline graphite to sp^2 a-C: In this stage the G peak shifts from 1600 to 1510 cm^{-1} and the I(D)/I(G) ratio decreases, which is a result of the enhanced creation of amorphous structures [21].

• **Stage 3:** from sp^2 a-C to sp^3 ta-C: In the final stage the main changes are the shift of the G-peak from 1510 to 1570 cm^{-1}, with a simultaneous decline of the D-peak due to the lack of sp^2 bonds in the material. The closer the end of the stage is approached, the more the I(D)/I(G) ratio is reduced until it eventually becomes zero and only the ta-C phase remains [21].

2.6 Elastic recoil detection analysis

Elastic recoil detection analysis (ERDA) is an ion beam analysis technique, which is used to analyse the elemental concentration depth profiles in thin films [42]. It was originally developed to detect H and other light elements. The principle of ERDA is based on the elastic scattering of heavy primary incident ions on a sample surface and the following detection of recoiling sample atoms [43]. The information of the targeted sample is carried by the sample particles themselves instead of the backscattered primary ions, as in Rutherford backscatter spectroscopy, for instance. This allows a more exact investigation of the particles compared to other detection techniques [43]. The schematic interaction of the incident ion and the target atom is shown in Fig. 2.17. There, M_1 and M_2 are the mass of the incident ion and the target atom, respectively, and Θ is the recoil angle of the scattering process.

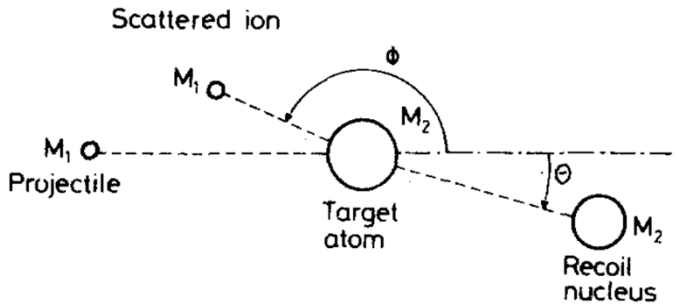

Figure 2.17: Schematic representation of the scattering process during ERDA [44].

The energy of the recoil nucleus E_1 which is transferred by projectile ions with the initial energy E_0 to sample atoms, is defined through equation [44]

$$E_1 = E_0 \frac{4M_1 M_2}{(M_1 + M_2)^2} \cos^2 \Theta. \tag{2}$$

The relation between the scattering angle ϕ and the recoil angle Θ characterises the geometry of the collision and is described by equation [44]

$$\cos^2 \Theta = \frac{(M_1 M_2)^2 - (M_1 \cos\phi \pm \sqrt{M_2^2 - M_1^2 \sin^2\phi})^2}{4M_1 M_2}. \tag{3}$$

By determining the kinetics, the loss of energy and the mass of the recoil target atoms, an elemental analysis as a function of the coating depth can be carried out through ERDA.

3 Experimental Details

3.1 Coating Deposition

3.1.1 Deposition System

All thin films for this work were deposited using the laboratory scale unbalanced magnetron sputtering system “Margot”, as shown in Fig. 3.1.

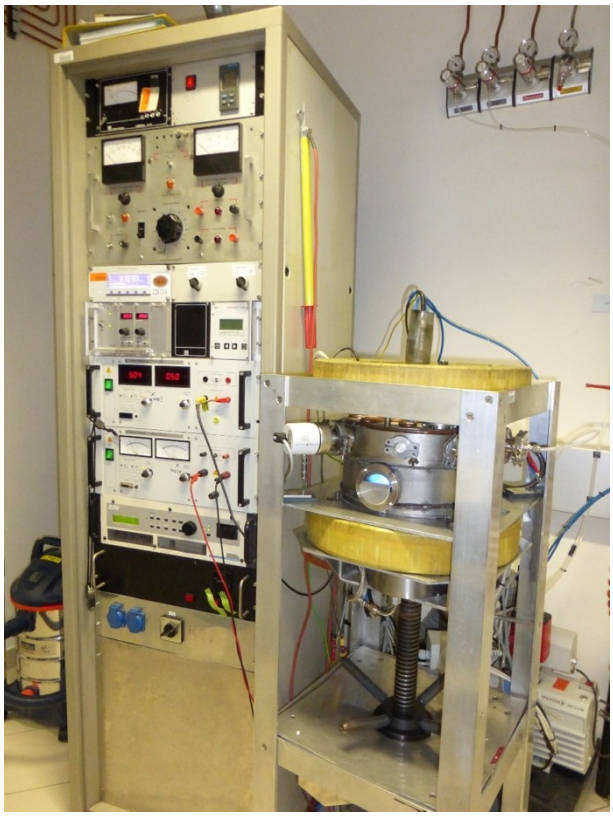

Figure 3.1: Magnetron sputter deposition system “Margot”.

The deposition chamber is a cylindrical stainless-steel vacuum chamber with the dimensions ø 300 mm × 140 mm and a volume of 10 l. The system contains NdFeB permanent magnets behind the target serving as a magnetron and external Helmholtz coils to create an additional magnetic field in order to influence the plasma. The device is equipped with an ENI DCG-150/75 generator which is able to supply a maximum power of 8000W. The pump system consists of a Pfeiffer DUO 20 M rotary vane pre-pump and a Pfeiffer “HiPace Turbomolecular” rotary pump. The target which was used for all experiments was a planar circular target produced by FHR (Ottendorf-Okrilla, Germany). The water-cooled target consists of a 150 mm diameter graphite plate with a thickness of 6 mm bonded onto a 4 mm molybdenum backing plate. The two plates were connected by a high temperature stable tin bonding layer. The carbon target had a purity of no less than 99.99 %. The substrate holder is mounted parallel

to the target surface at a distance of 80 mm. Inside the deposition chamber, there is a shutter to separate the target and the substrate during the pre-sputter and etching process.

3.1.2 Sputter Deposition Procedure

Within this thesis, all thin films were deposited on single crystal silicon strips in (100) orientation with the dimensions 20 mm × 7 mm × 0.380 mm. Prior to deposition, the substrates were ultrasonically cleaned in acetone and ethanol for 10 min each and dried by a hot air gun. Additionally, they were polished with a laboratory wipe and cleaned with pressured air to ensure a clean substrate surface. For each deposition experiment four samples were placed on the sample holder. Their arrangement is shown in Fig. 3.2. The substrate temperature was measured with a shielded K-type thermocouple (ø 1.5 mm) attached to a steel blank located on the sample holder. No external substrate heating was applied during the deposition.

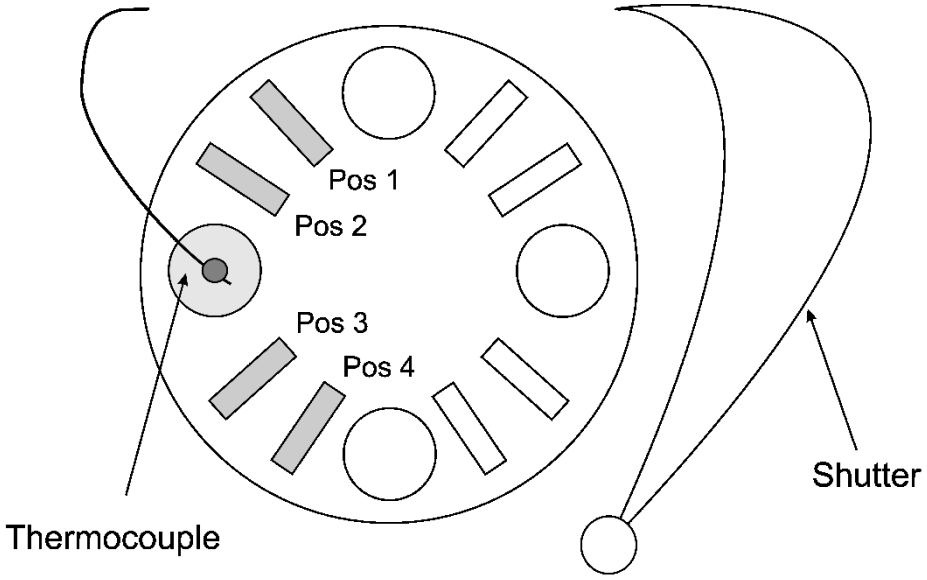

Figure 3.2: Substrate deposition arrangement.

The deposition chamber was evacuated to a base pressure of < 2×10^{-3} Pa. The initial step was the pre-sputtering of the target to remove any contaminated layer on the target surface. This was performed in an Ar atmosphere with a gas flow of 15 sccm. The current was set to 1.5 A and the process was performed for a duration of 10 min. The second step was a cleaning of the substrate surface by the use of a plasma-etching procedure. This was achieved by igniting a plasma between the substrate and the shutter for 20 to 30 min. The voltage was set to -1250 mV and the current to 20 mA. The etching process was performed in an Ar atmosphere with a gas flow between 160 and 170 sccm. After these first two steps the actual deposition was started. A carbon base layer was deposited at first to ensure a good film-substrate adhesion. It was deposited in an Ar atmosphere for all experiments. The deposition time of the base

layer was set to an eighth of the overall deposition time and consequently varied from 3.75 to 23.5 min. All base layers were deposited without any bias voltage applied. The actual deposition experiments were performed in Ar, Ne and He atmospheres. The gas flow during deposition was adapted to guarantee a constant chamber pressure of 1 Pa for Ar and He and 1.25 Pa for Ne, which was established by gas flows of 50, 68 and 115 sccm for Ar, Ne and He, respectively. The coatings were synthesised at different power densities calculated on the basis of the erosion zone of 120 cm^2 and ranged from 4.4 to 28 W/cm^2. The power density was kept constant during deposition. In some experiments an additional bias voltage was added in the deposition process. The deposition time increased with decreasing power density and varied between 30 and 188 min (including the deposition of the base layer) in order to obtain coatings with a thickness of about 2 μm. The detailed deposition parameters are summarized in Tab. 3.1.

Table 3.1: Deposition parameters.

Gas	bias voltage [V]	power density [W/cm²]	deposition time [min]
Argon	-25 (floating potential)	4.4	188
		10.3	80
		16.2	52
		22.1	38
		28.0	30
	-50	4.4	188
		10.3	80
		16.2	52
		22.1	38
		28.0	30
	-68	10.3	80
	-100	10.3	80
Neon	-61 (floating potential)	4.4	188
		10.3	80
		16.2	52
		22.1	38
		28.0	30
He	-100 (floating potential)	10.3	80

3.2 Coating Characterization

3.2.1 Scanning Electron Microscopy

The cross sections of the deposited thin films were investigated using a scanning electron microscope (SEM, Zeiss Evo-50). To be able to perform cross sectional analyses, the samples were carefully split in the middle by hand, without damaging the sample surface. The base layer and the coating thickness were determined from the SEM cross sectional images. The chemical composition of the thin films was analysed by an energy dispersive X-ray emission spectroscopy system (EDX, Oxford Instruments INCA), which is attached to the scanning electron microscope.

3.2.2 X-Ray Diffraction

To investigate the microstructure of the thin films, X-ray diffraction (XRD) measurements were performed. The scans were carried out with a Bruker-AXS D8 Advance diffractometer. All coatings were measured with Cu K_α radiation with a wavelength of 0.154 nm. The tube current was set to 40 mA and the tube voltage was 40 kV. The diffractograms were recorded in grazing incidence mode with an incidence angle of 2° and a scan range from 20 to 100°. The scanning step size was 0.02° with a step time of 1.2 s, resulting in a scan speed of 1 °/min. The recorded patterns were compared with reference patterns from the database of the International Centre for Diffraction Data (ICDD).

3.2.3 ERDA

The ERDA measurements were carried out at the Helmholtz-Centre Dresden-Rossendorf using a 43 MeV $^{35}Cl^{+7}$ ion beam. The angle between the sample normal and the incoming beam was set to 75°, the scattering angle was set to 31°. The investigated area was about 1.5 × 1.5 mm^2. The recoiling sample ions were detected using a Bragg ionization chamber. H particles were detected with a separate solid state detector at a scattering angle of 41°. An 18 µm thick Al foil was used in the detector to stop the scattered primary beam and heavy recoil ions.

3.2.4 Raman Spectroscopy

The Raman spectroscopy measurements were carried out by using a Horiba Jobin Yvon LabRam-HR800 Raman spectroscope equipped with a frequency-doubled Nd-YAG laser (532.068 nm, 100 mW). The laser intensity was measured between the wavenumbers 500 and 2200 cm^{-1}. Different filters were used to reduce the intensity of the laser to avoid damaging of the thin film surface. The recorded Raman-curves were analysed with the software Origin by fitting two Gaussian peaks at 1350 cm^{-1} and 1580 cm^{-1}.

3.2.5 Wafer Curvature Measurement

The biaxial stress measurements were carried out with the wafer curvature device “Mutti 2000” by Winkler [45] at room temperature. In this method, the stresses are determined by measuring the curvature of the film-substrate composite. A deposited thin film shows internal stresses which results in a deformation of the film-substrate composite. This deformation results in a curvature, which depends on the residual stress state of the composite. Compressive stresses lead to a concave curvature of the sample whereas tensile stresses lead to a convex curvature. The samples were placed on top of a glass plate and analysed at room temperature. Two parallel laser beams are used to measure the radius of curvature. These laser beams have a known distance d_0 and are projected onto the sample from above. The beams are first reflected on the sample surface to a mirror and then reflected again onto the measuring plate. By measuring the distance after reflection d_1 and the total laser beam path h, the curvature radius R can be calculated with:

$$R = \frac{2hd_o}{d_1 - d_0}. \tag{4}$$

The total stress in the coating σ can then be determined with the modified Stoney equation [46]

$$\sigma = M \frac{t_s^2}{6t_c} \frac{1}{R}, \tag{5}$$

with t_s being the thickness of the substrate and t_c being the thickness of the coating. M is the biaxial modulus of the (100) oriented silicon substrate $M_{(100)}$ = 180 GPa.

3.2.6 Electrical Resistivity Survey

The sheet resistivity of all thin films was measured by the four-point technique with a “Jandel Multi Height Probe”. Each measurement was taken in the centre of the sample. The four measurement tips were aligned parallel to the length of the substrate and were brought in contact with the thin film surface without any mechanical loading of the film itself. From the measured voltage V the sheet resistivity R_s can be calculated through the equations

$$\rho = \frac{\pi t}{\ln 2} \left(\frac{V}{I}\right) \tag{6}$$

and

$$R_s = \frac{\rho}{t}, \tag{7}$$

where ρ is the bulk resistivity, I is the applied current and t is the film thickness.

3.2.7 Nanoindentation

A nanoindenter system UMIS (Ultra Micro Indentation System) from Fischer-Cripps laboratories was used to determine the hardness and Young´s modulus the thin films. All measurements were performed with a Berkovich diamond-indenter, which allows a simultaneous measurement of the load and penetration depth. The coating samples were mounted onto a specimen holder and acclimatised in the chamber to avoid thermal drift. A plateau test from 5 to 15 mN in steps of 0.5 mN was carried out for each sample. The resulting load-displacement curves were analysed using the Oliver and Pharr method [47] using the IBIS software provided by the manufacturer. To reach reasonable statistics, a minimal of 14 indents per sample were used for the analysis.

4 Results

4.1 Discharge Properties

Figure 4.1 displays the target voltage as a function of the power density for all three inert gases used. The coatings which were deposited in a 1 Pa Ar atmosphere, both at floating potential and at an applied bias voltage of -50 V, show a steady increase of the discharge voltage with increasing power density. The two curves are nearly congruent and their discharge voltage values range from approximately -540 to -630 V. Also, when the bias voltage was raised to -68 and -100 V at a power density of 10.3 W/cm^2, no deviation from this voltage characteristics was observed. The discharge values for the depositions in a 1.25 Pa Ne atmosphere at floating potential are lower than for the 1 Pa Ar atmosphere, ranging from -420 to -470 V. The curve shows a slight increase for the power density rising from 4.4 to 10.3 W/cm^2, above which it remains constant up to the power density of 28 W/cm^2. The voltage for the depositions in the 1 Pa He atmosphere at floating potential showed the lowest discharge voltage of approximately -400 V. No pronounced change with power density was observed.

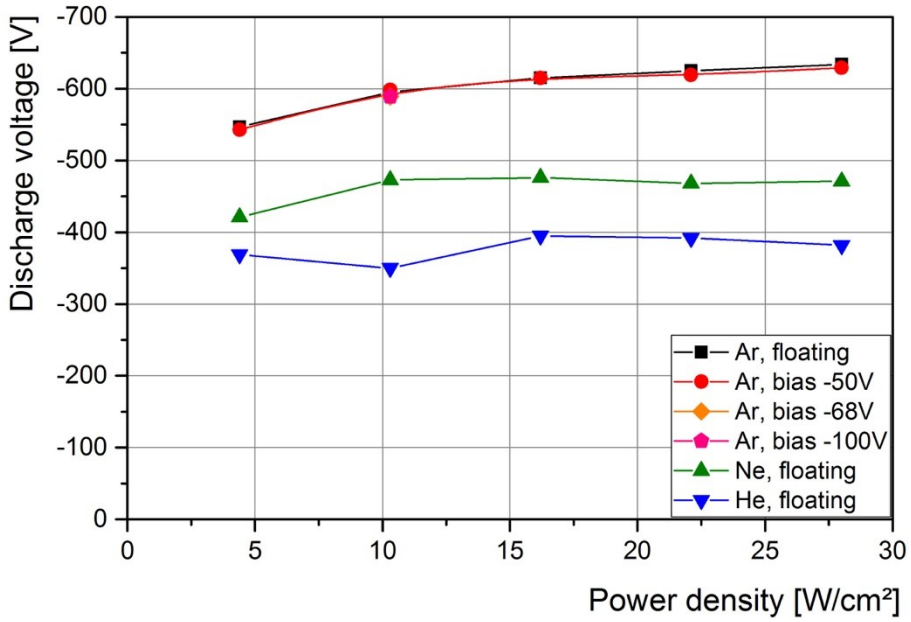

Figure 4.1: Target voltage as a function of power density for different atmospheres at different bias voltages.

The substrate ion current displayed in Fig. 4.2 was determined as the current that was carried by the bias generator. The ion current at an applied bias voltage of -50 V shows a linear rise with power density and ranges from 90 to 440 mA. As can be seen from the graph, the bias voltage only has little influence on the substrate ion current. When the bias voltage is raised

to -68 and -100 V at a power density of 10.3 W/cm^2, the substrate ion current increases only slightly to 180 and 190 mA, respectively. In the case of the experiments in Ar, Ne and He atmospheres, the substrate holder was set at floating potential and consequently showed a total substrate ion current of 0.

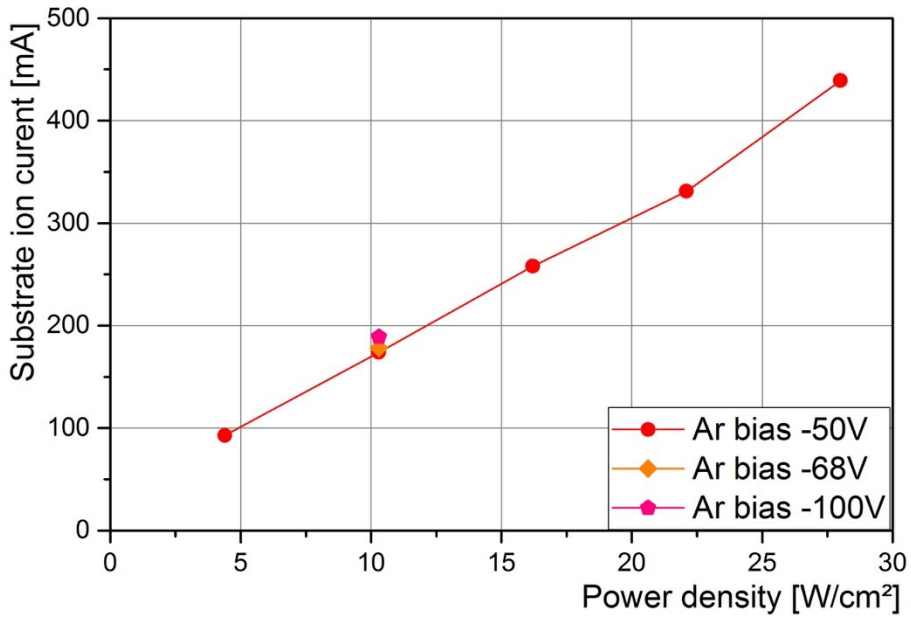

Figure 4.2: Substrate ion current for the depositions in Ar atmosphere.

4.2 Substrate Temperature Measurements

Figure 4.3 shows the time dependence of the substrate temperature as a function of the power density for samples deposited at floating potential in a) Ar and b) Ne atmospheres. During the etching process the substrate temperature increases to values between 60 and 80 °C. Hence, the temperature curves in Fig. 4.3 start at elevated temperatures and not at room temperature. As expected, the substrate temperature increases during the deposition. The temperature curves in Fig 4.3 show that the substrate temperature of thin films, deposited between power densities of 10.3 and 28 W/cm^2, peak at the very end of the deposition. However, the temperature curve of the sample deposited at a power density of 4.4 W/cm^2 shows that the substrate temperature saturates and remains constant from minute 60 onwards and reaches a maximum temperature of 80 °C for the samples deposited in Ar and 120 °C for those deposited in Ne. The data shows that the higher the power density during the deposition is, the higher the thermal load of the growing film. The samples deposited in Ar, as well as those deposited in Ne atmosphere, reached their maximum substrate temperature at the end of the deposition at the power density of 28 W/cm^2 at values of 170 and 270 °C, respectively. The temperature measurements in Fig. 4.3 b) show a noticeable change of the curve gradients after 1/8 of the deposition time. This corresponds to the change from the Ar gas used for the deposition of the base layer to Ne, which was used for the remaining deposition.

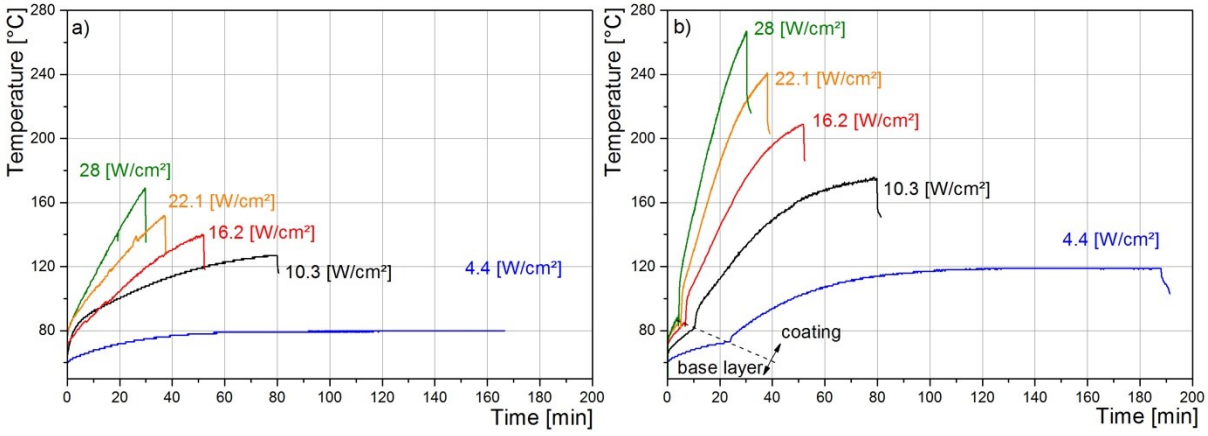

Figure 4.3: Substrate temperature curves for coatings deposited in a) Ar and b) Ne atmospheres both at floating potential. The dashed line in b) refers to the change of deposition gas from Ar to Ne.

Figure 4.4 a) shows temperature curves of depositions carried out in different atmospheres. The data used for this graph were all taken during depositions at a power density of 10.3 W/cm^2 and floating potential. The substrate temperature of the coatings depends on the used deposition gas. Samples deposited at floating potential in He atmosphere reach a much higher

substrate temperatures of 280 °C, while the samples of those films deposited in Ne and Ar atmosphere approach substrate temperatures of 175 and 130 °C, respectively. The samples deposited in Ne and He atmosphere show a sudden rise in temperature after the deposition of the base layer. For the He curves, this occurs from approximately 85 to 125 °C and the Ne curves show this increase from 80 to 95 °C. The influence of an applied bias voltage on the substrate temperature is presented in Fig. 4.4 b). The curves depicted in the diagram stem from depositions conducted at a power density of 10.3 W/cm^2 in Ar atmosphere. The curves show, that the temperature rises with increasing bias voltage. The maximum temperature ranged from approximately 130 °C at floating potential to 190 °C at an applied bias voltage of -100 V. The deposition with a bias potential of -100 V shows a distinct rise in temperature after the deposition of the base layer.

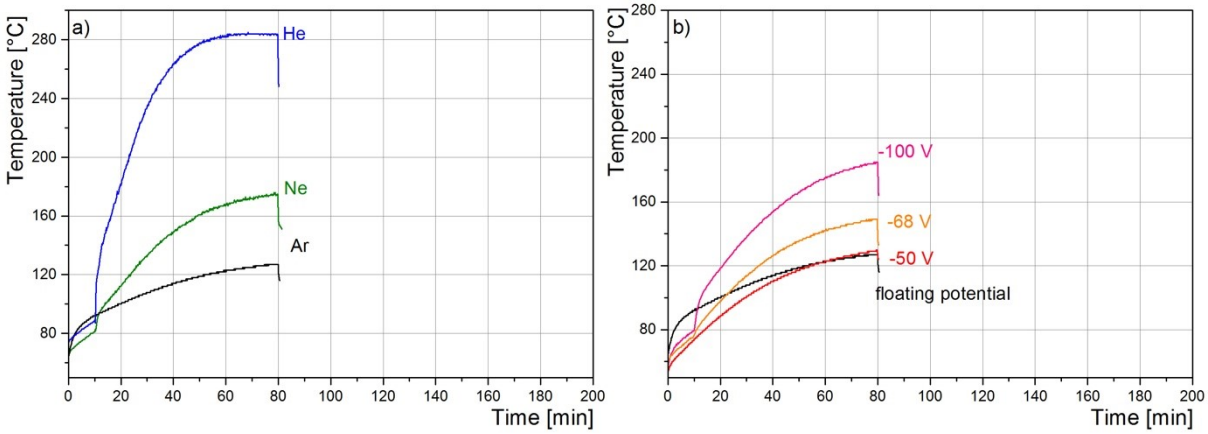

Figure 4.4: Substrate temperature curves of the deposition processes carried at a power density of 10.3 W/cm^2 in a) different atmospheres at floating potential and b) at different bias voltages.

4.3 Deposition Rate

The deposition rate of the investigated coatings at different power densities is displayed in Fig. 4.5. It can be seen that the deposition rates of all samples show a significant rise over the power density. The deposition rate increases more strongly than anticipated and deviates from linear behaviour with rising power density. Coatings deposited in an Ar atmosphere at floating potential showed the highest deposition rates ranging from 0.011 to 0.093 μm/min. Applying a bias voltage leads to a minor decrease of the deposition rate. The samples deposited in Ar with an applied bias voltage of -50 V exhibited slightly lower deposition rates, with a maximum of 0.083 μm/min at 28 W/cm². Further increasing the bias voltage has no effect on the deposition rate. The three films deposited in Ar atmosphere at bias voltages of -50, -68 and -100 V and a power density of 10.3 W/cm² showed almost the same values. The experiments conducted in Ne atmosphere yielded a lower deposition rate than those performed in Ar. Their deposition rate values range from 0.008 to 0.062 μm/min. The sample grown at 10.3 W/cm² in He showed the lowest deposition rate at that power density with a value of 0.017 μm/min.

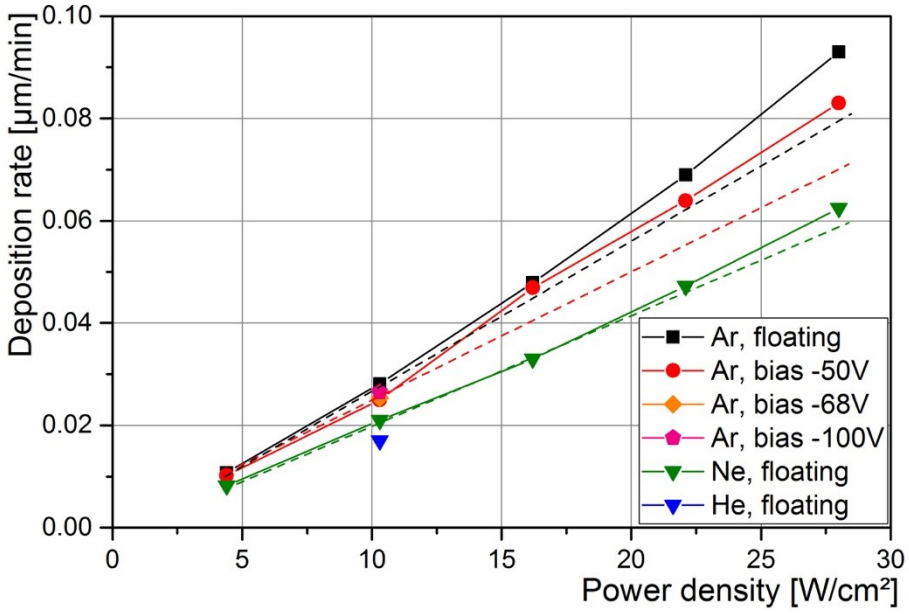

Figure 4.5: Deposition rate of the investigated coatings as a function of power density. The dashed lines refer to the linear courses of the deposition rate.

4.4 SEM cross sections

The SEM cross section images were used to determine the thickness of the coatings, the deposition rate and to characterize the microstructure. Figure 4.6 represents samples grown in Ar and Ne atmospheres at floating potential and different power densities. The interface between the substrate and the coating can clearly be seen in Fig. 4.6 a). The depicted film was deposited in Ar atmosphere at floating potential and at a power density of 4.4 W/cm^2. The substrate possesses a darker fracture surface, while the coating appears brighter with a smooth and featureless fracture surface. The coating which is seen in Fig. 4.6 c) was deposited at a higher power density of 28 W/cm^2. It demonstrates the rise of the coating thickness at higher power densities.

Figure 4.6 b) shows the coating deposited in Ne atmosphere at 4.4 W/cm^2. Coating, base layer and substrate can be clearly distinguished. Figure 4.6 d) exemplifies a film deposited at a power density of 28 W/cm^2. Again, there is still a clear separation of the coating, the substrate and the base layer. No coating presents any indication of grain boundaries. This confirms that all of the deposited films possess an amorphous structure.

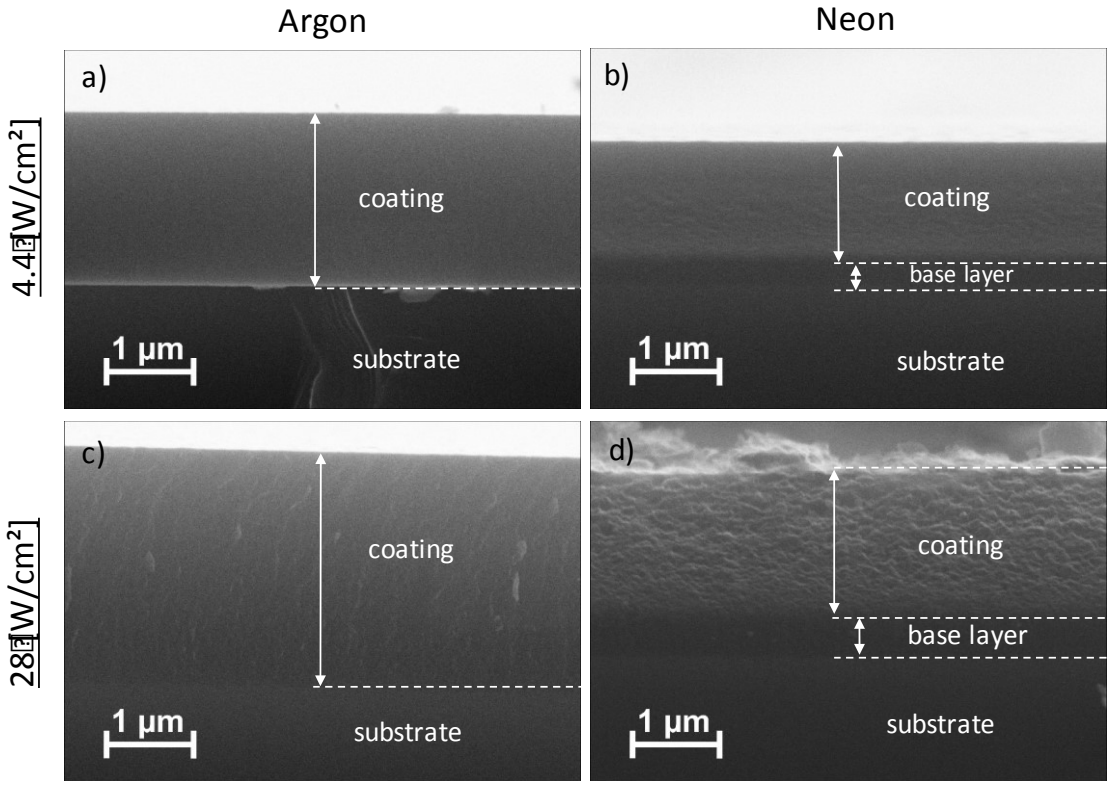

Figure 4.6: SEM fracture cross sections of films deposited in Ar and Ne atmospheres with floating potential at different power densities.

Figure 4.7 shows thin films deposited in Ar atmosphere at a power density of 10.3 W/cm^2. The applied bias voltage during the deposition process increases from Fig. 4.7 a) to Fig 4.7 d). It can be seen that the coating thickness slightly decreases with increasing bias voltage, which is indicative for a lower deposition rate. The fracture surface possesses a light texture in Fig 4.7 a) to c). The Ar sample shown in Fig. 4.7 d) shows a coating, whose featureless cross section is similar to the surfaces of the Ne samples. Also, there is a clear separation between the base layer and the coating, which does not appear in any other Ar sample. None of the samples shows any distinct grains and therefore it can be concluded that all coatings have an amorphous structure, regardless of the applied bias voltage.

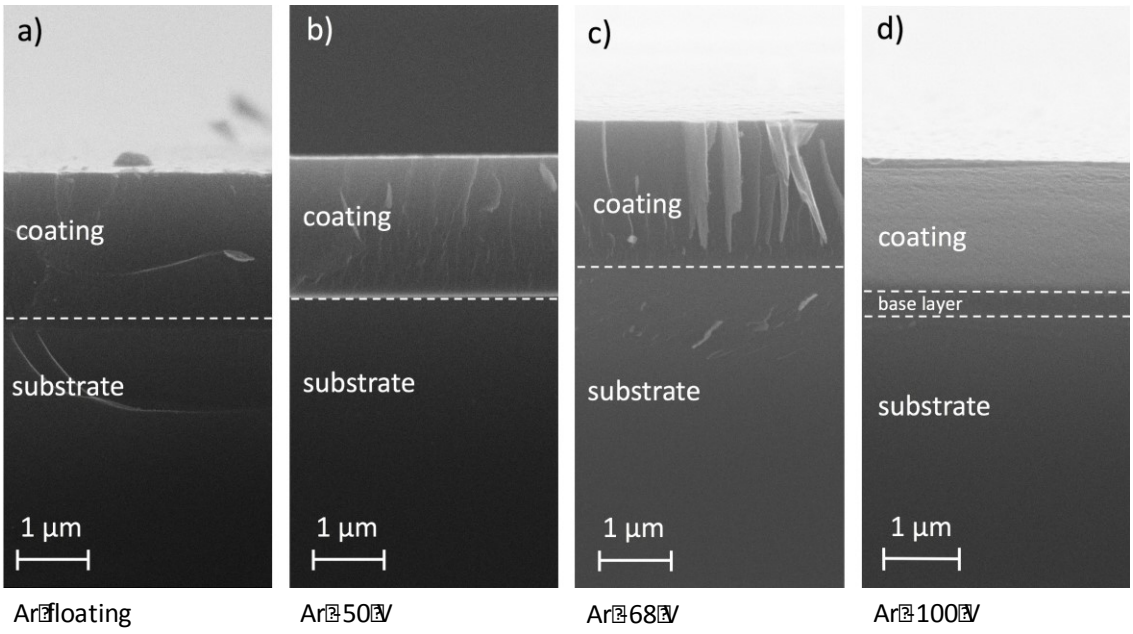

Figure 4.7: SEM fracture cross sections of films deposited in Ar atmosphere at a) floating potential and bias voltages of b) -50 V, c) -68 V and d) -100 V.

4.5 X-Ray Diffraction

XRD measurements were performed for all samples to determine the crystal structure of the carbon thin films. They all show the typical pattern of an amorphous structure regardless of varying deposition parameters. Figure 4.8 displays the X-ray diffractograms of coatings deposited at different power densities in Ar atmosphere without bias potential applied. The curves do not change significantly with varying power density. All five curves only show a slight indication of a peak at about 57°.

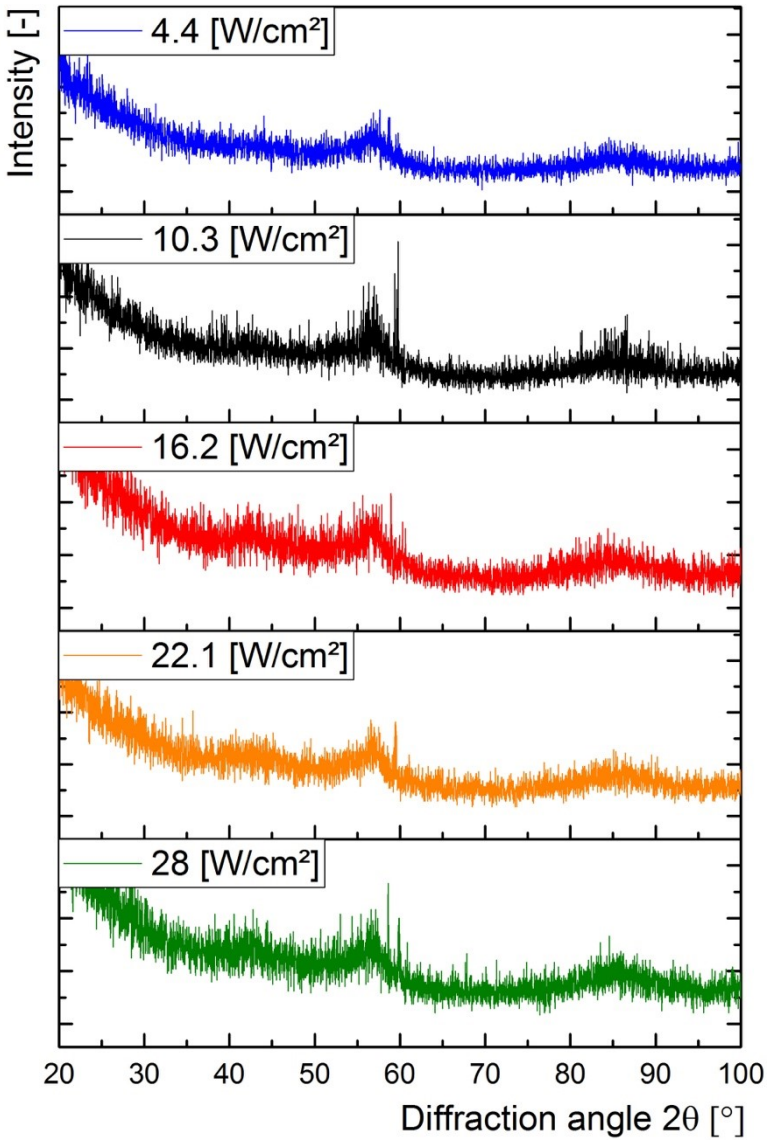

Figure 4.8: X-ray diffractograms of carbon thin films deposited at different power densities in Ar atmosphere at floating potential.

X-ray diffractograms of coatings deposited in different atmospheres and bias potentials at a power density of 10.3 W/cm^2 are shown in Fig. 4.9. Samples represented by the first three curves were deposited in Ar atmosphere but at different bias voltages. Neither the bias voltage, nor the deposition gas results in any noticeable differences in the patterns. The indication of a peak can also be seen in these five curves at around 57°.

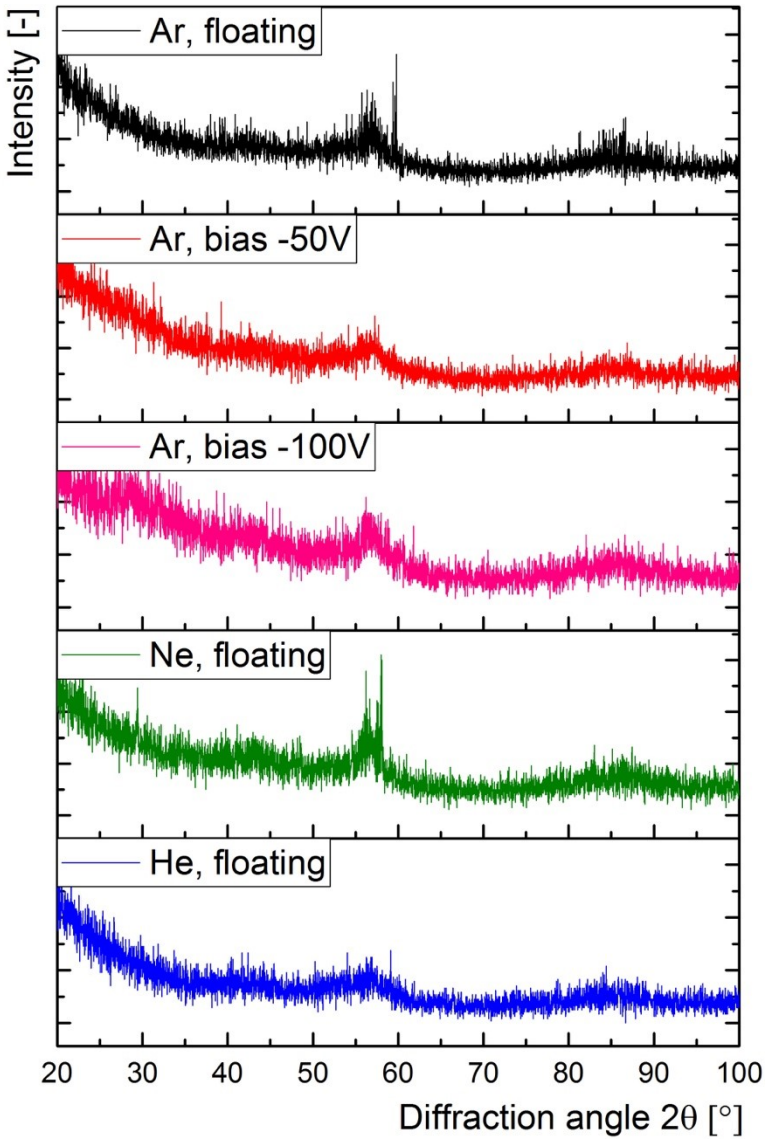

Figure 4.9: X-ray diffractograms of carbon thin films deposited at 10.3 W/cm^2 in different atmospheres and at different bias voltages.

4.6 Raman Spectroscopy

Figure 4.10 shows a typical example of a measured Raman spectrum of an a-C film. The red dashed line in the diagram represents the Gaussian fit of the D-peak, while the green, dotted line represents the Gaussian fit of the G-peak. The intensity of the D and G-peak and the Raman shift position of the G-peak were measured from this and similar curves and used for further analysis.

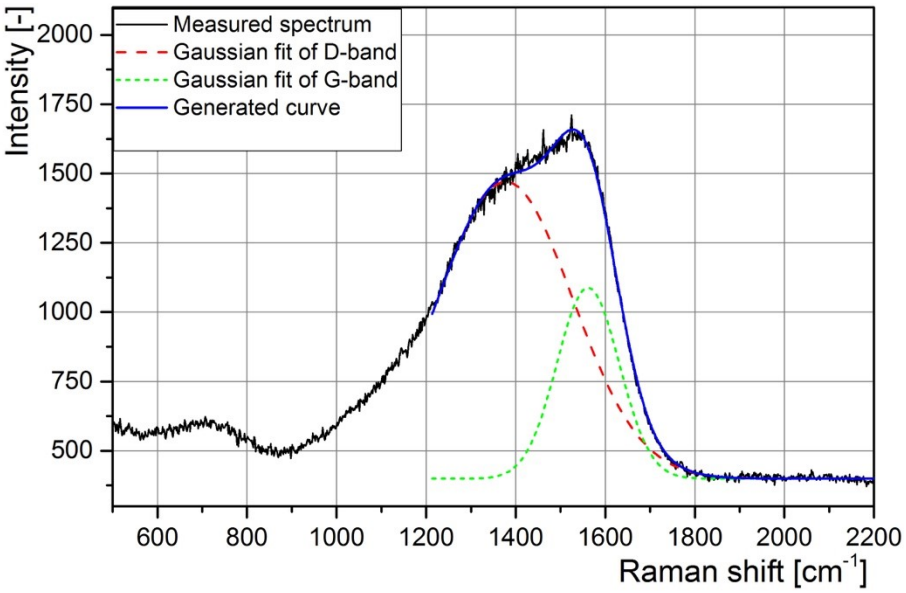

Figure 4.10: Raman spectrum of a measured a-C thin film deposited at a power density of 10.3 W/cm^2 in Ar atmosphere and without bias voltage.

The position of the G-peak in the Raman shift measurement as a function of power density is presented in Figure 4.11 a). The G-peak position of all samples is shifted towards higher values with increasing power density. The films deposited in Ne atmosphere show a similar trend as the coatings deposited in Ar atmosphere. Their positions, however, lie at slightly higher values, ranging from 1565 to 1578 cm^{-1} while the measurements of the samples deposited in Ar atmosphere range from 1556 to 1574 cm^{-1}. The sample deposited in He atmosphere at a power density of 10.3 W/cm^2 shows the G-peak position with the highest value of 1580 cm^{-1}. All samples deposited in Ar atmosphere at 10.3 W/cm^2 show a similar G-peak position. These measurements indicate that an applied bias voltage does not affect the G-peak position.

Figure 4.11 b) summarizes the I(D)/I(G) intensity ratio of the investigated films over the power density. Similar to the G-peak position, all samples show an overall rise of the intensity ratio with increasing power density. The samples deposited in Ne atmosphere yield the most pronounced increase of the ratio over the power density ranging from 1.20 to 1.66. The films deposited in Ar at floating potential show a marginal rise of the intensity ratio varying from

1.43 to 1.56. In contrast to the samples deposited in Ar atmosphere and with an applied bias voltage of -50 V a stronger increase was obtained, similar to the samples deposited in Ne, reaching the highest ratio of 1.88 at a power density of 22.1 W/cm^2. The coating deposited in He atmosphere at floating potential and a power density of 10.3 W/cm^2 shows roughly the same value as the sample deposited in Ne atmosphere with a ratio of 1.39. The samples grown at the power density of 10.3 W/cm^2 demonstrate that the ratio rises significantly with increasing bias voltage. The sample deposited at floating potential had the lowest ratio of 1.5, while the coating synthesized at -68 V and -100 V possessed ratios of 1.8 and 1.76.

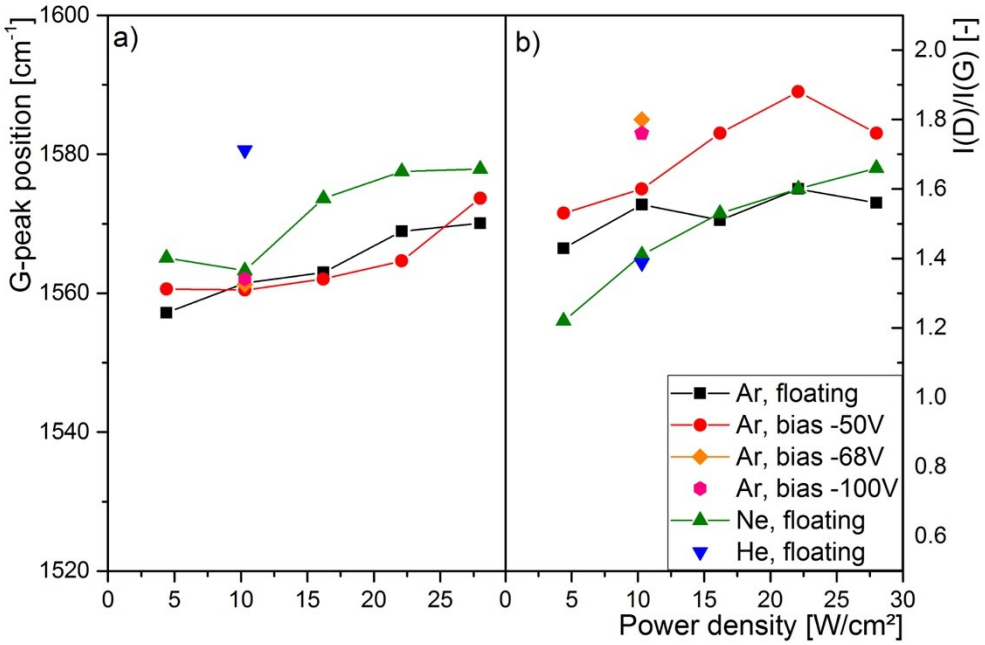

Figure 4.11: a) Raman G-peak position and b) I(D)/I(G) ratio of a-C thin films deposited in different atmospheres and at different bias voltages in dependence on the power density.

4.7 Wafer Curvature Measurement

The residual film stress as a function of the power density is illustrated in Fig. 4.12. The diagram shows the stress values of coatings deposited at various bias voltages in Ne and Ar atmospheres. All analysed samples exhibit compressive stress. Those deposited in Ar atmosphere at floating potential exhibit the lowest residual stress, which remains approximately constant with power density at stress values between -300 and -400 MPa. The coatings deposited in Ar atmosphere at a bias voltage of -50 V have slightly higher residual stress. The stress decreases slightly with increasing power density and ranges from -1600 to -600 MPa. The samples deposited in Ar atmosphere at even higher applied bias voltages and a power density of 10.3 W/cm^2 show that the residual stress value increases with increasing bias voltage. While the sample deposited at a power density of 10.3 W/cm^2 in Ar atmosphere at floating potential has a stress of -400 MPa, the sample deposited at -100 V possesses a stress of -2700 MPa. In general, the coatings deposited in Ne at floating potential show a decrease of residual stress over the power density. Their stress values range from -1600 to -2900 MPa. The residual stress of the thin films deposited in He atmosphere could not be measured due to insufficient coating adhesion.

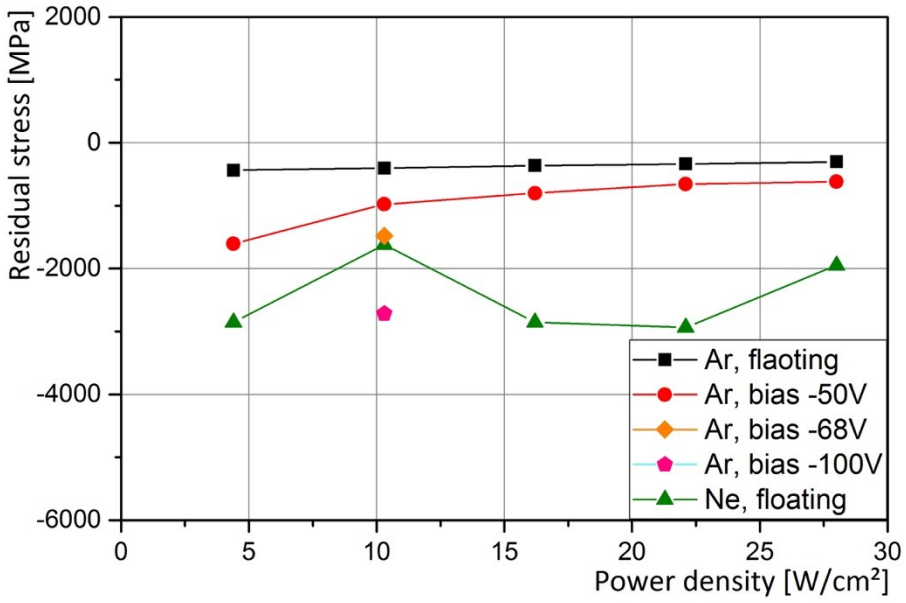

Figure 4.12: Residual stress of coatings deposited at different parameters in various atmospheres.

4.8 Nanoindentation

The elastic modulus and the hardness of the films were determined by nanoindentation. The results are displayed in Fig. 4.13 as a function of power density with error bars indicating the standard deviation of the measurements. Overall, the coatings deposited in Ne and Ar atmospheres at floating potential show a decline of the elastic modulus with increasing power density. The film deposited in Ar atmosphere at a power density of 10.3 W/cm^2 and an applied bias voltage of -100 V shows the highest elastic modulus of 300 GPa. The sample deposited in He atmosphere at floating potential and the same power density possesses the lowest elastic modulus of 96 GPa. The films grown in Ar atmosphere at a power density of 10.3 W/cm^2 demonstrate that the elastic modulus increases with increasing bias potential.

Figure 4.13 b) illustrates the hardness of the thin films as a function of power density. The hardness of the investigated samples shows a similar behaviour as the elastic modulus, i.e. a decrease with increasing power density. The film deposited in Ar atmosphere with an applied bias voltage of -100 V possesses the highest hardness value of 33 GPa and the coating deposited in He atmosphere at floating potential has a measured hardness of 9.4 GPa. The hardness values of the coatings deposited in Ar at a power density of 10.3 W/cm^2 show a significant rise with increasing bias voltage.

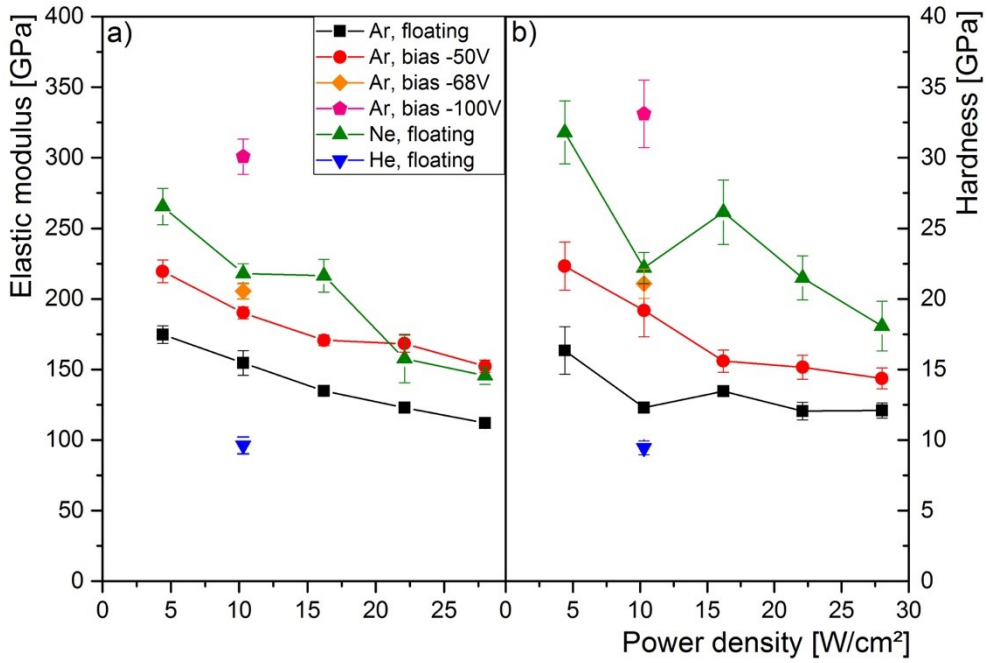

Figure 4.13: Elastic modulus a) and hardness b) of carbon thin films deposited in various atmospheres and at different bias voltages as a function of power density.

4.9 Electrical Resistivity Survey

The results of the sheet resistivity measurements are displayed as a function of power density in Fig. 4.14. The coatings deposited in Ar atmosphere at floating potential and a power density of 4.4 W/cm^2 show the highest electrical resistivity of all samples with a value of 0.16 Ωcm. Overall, a gradual decline with the power density is present. The coatings deposited in Ar atmosphere at an applied bias voltage of -50 V show lower resistivity values. The electrical resistivity gradually decreases between 4.4 and 16.2 W/cm^2 and remains constant at higher power densities. The values for the -50 V samples range from -620 to -1600 Ωcm. In general, it can be said that the electrical resistivity decreases with an increase of the applied bias voltage. The samples deposited at bias voltages of -68 and -100 V show the lowest electrical resistivity values of 0.016 and 0.015 Ωcm, respectively.

Similar to the coatings synthesized in Ar, the films deposited in Ne atmosphere show a decrease of electrical resistivity with rising power density. Their dependence is nearly congruent with that of the coatings deposited in Ar atmosphere at a bias voltage of -50 V and the obtained values range from 0.01 to 0.08 Ωcm. The electrical resistivity of the coatings deposited in He atmosphere could not be measured due to insufficient coating adhesion.

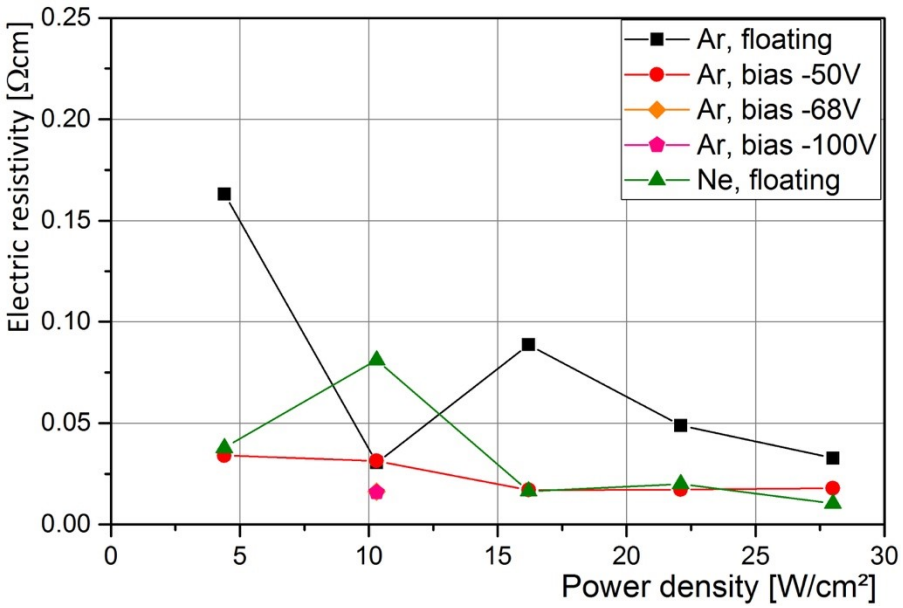

Figure 4.14: Electrical sheet resistivity of coatings deposited in Ar and Ne atmospheres and varying bias voltage as a function of power density.

4.10 Chemical composition

The chemical composition of the films was determined via ERDA and EDX and the obtained results are compared in the following section. The chemical compositions determined by ERDA are listed in Tab. 4.1. The analysis shows that the main impurities of the carbon coatings are Ar, O, H and a marginal amount of N. The Ar content in the deposited films decreases with increasing power density, while the O content simultaneously increases. Furthermore, the Ar content in the films grown in Ar atmosphere rises with increasing power density, while the O content slightly decreases. The H content of the films remains constant regardless of the alteration of power density and bias voltage. The films deposited in Ar atmosphere contain the least amount of impurities, while the sample grown in He atmosphere yielded the highest concentration. Samples deposited in Ar atmosphere show a rising Ar content with increasing bias voltage. For those films deposited in Ne and He atmosphere also a small concentration of Ar could be determined. This is due to the base layer, which was deposited in Ar atmosphere. The films deposited in Ar atmosphere show rather low O concentrations, while the He sample has a much higher concentration. For the samples grown in Ne atmosphere, the highest O content was obtained. Furthermore, the samples deposited in Ar show the lowest concentration of H, which reaches much higher values in those films grown in Ne and even more in He. The N impurities in the coating are overall constant for every measured sample. The values obtained for samples that show Ar fractions below 0.2 at % are not precise due to the detection method, but can be used for a comparison. The He which may be present in the film deposited in He could not be detected with the detector system used.

Table 4.1: Summary of ERDA results obtained for carbon coatings deposited in Ar, Ne and He atmosphere with varying parameters.

Gas	Bias voltage [V]	Power density [W/cm^2]	C [at %]	Ar [at %]	Ne [at %]	O [at %]	H [at %]	N [at %]
Ar	floating	4.4	95.5	0.71	-	0.67	2.8	0.27
Ar	floating	10.3	97.1	0.36	-	0.74	1.6	0.19
Ar	floating	22.1	94.5	0.14	-	1.5	3.6	0.14
Ar	floating	28	94.4	0.09	-	1.5	3.8	0.12
Ar	-50	10.3	94.6	3.1	-	0.38	1.9	0.16
Ar	-100	10.3	95.2	4	-	0.15	0.55	0.14
Ne	floating	10.3	88.3	0.04	0.88	2.3	8.1	0.2
Ne	floating	28	88.4	0.1	0.48	3.3	7.6	0.19
He	floating	10.3	81.9	0.03	-	1.6	16	0.55

In general, the values determined via EDX differ from those determined by ERDA, but show similar trends. The absolute values of the EDX measurements, however, have to be regarded with caution due to the high inaccuracy in the quantitative analysis for light elements.

The inert gas content of the a-C films versus power density is presented in Fig. 4.15. Figure 4.15 a) demonstrates the Ar and Ne content detected by ERDA. The solid symbols stand for the Ar content of the samples, while the open symbols represent the Ne content (only detected in those samples deposited in Ne atmosphere). The Ar and Ne content slightly decreases with increasing power density. The samples deposited at a power density of 10.3 W/cm^2 indicate that the Ar incorporation increases with rising bias voltages. Figure 4.15 b) shows the inert gas content determined by EDX. The films deposited in Ar atmosphere show comparable values and a similar dependency on the power density as when measured by ERDA, while those obtained for Ne show strong fluctuations and are on average higher than for the comparable films grown in Ar.

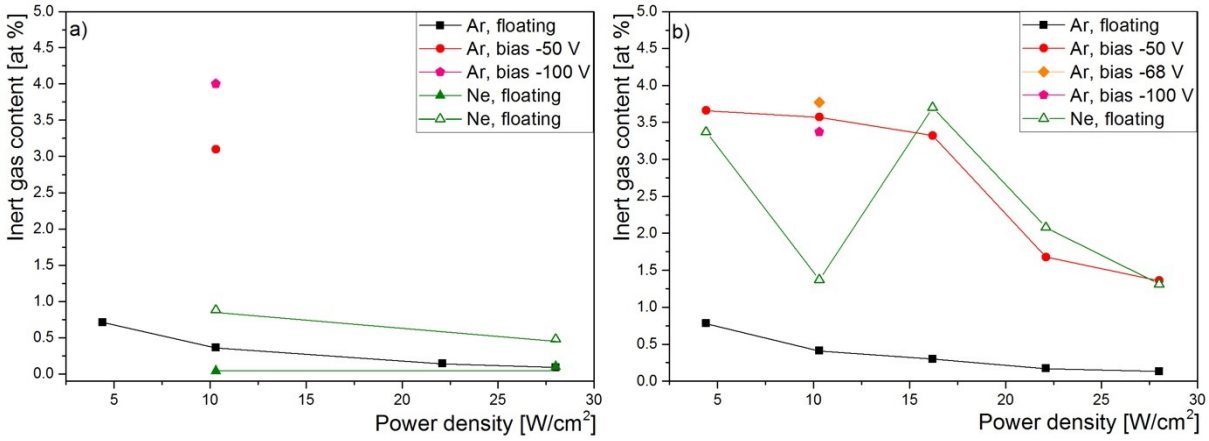

Figure 4.15: The inert gas content of a-C thin films measured with a) ERDA and b) EDX. The solid symbols refer to the Ar content, while the open symbols represent the Ne content.

Figure 4.16 presents the O concentration measurements of a) ERDA and b) EDX illustrating that the O content increases slightly at higher power densities. The measurements of the samples deposited at a power density of 10.3 W/cm^2 show that not only does the O content rise with decreasing bias voltage, it also rises when using He and Ne as a process gas. The O content detected by EDX generally lies at much higher values than for ERDA, which is most probably a result of the measurement inaccuracy. Figure 4.16 b) shows that the O content increases with increasing power density. The thin films deposited in Ar at floating potential show much higher values than the other samples deposited in Ar atmospheres and also than those synthesized using the other two gases.

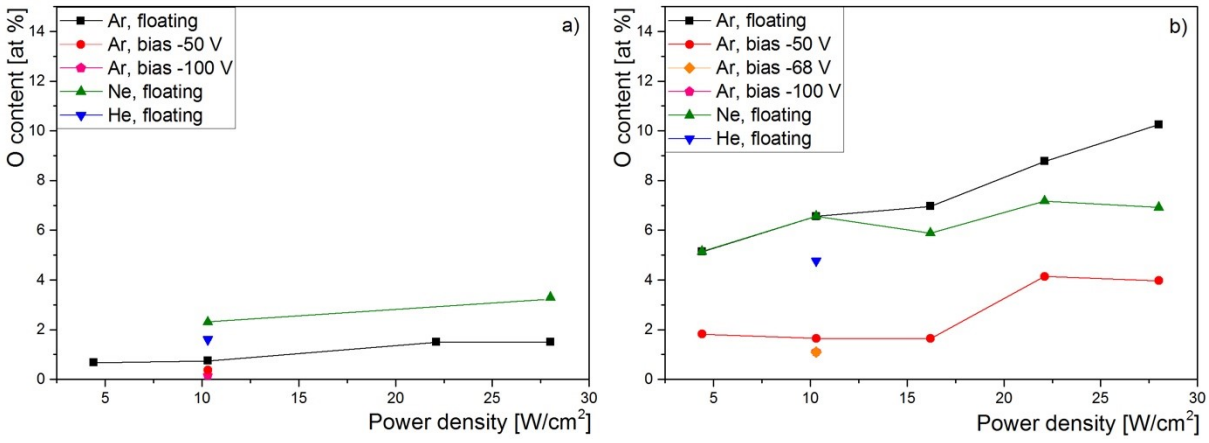

Figure 4.16: O content in the a-C thin films determined with a) ERDA and b) EDX.

The concentration of H in the film was only detectable using ERDA. The H content of the coatings remains constant over the power density, which is demonstrated in Fig. 4.17. The coatings deposited in Ar atmosphere possess the lowest concentration of H, while the sample deposited in He has the highest value. The films deposited in Ar atmosphere at a power density of 10.3 W/cm^2 show no significant change of the H concentration, when the applied bias voltage is varied. Overall, the H content of the films is approximately twice as high as the O content. This indicates that both impurities originate from H_2O vapour.

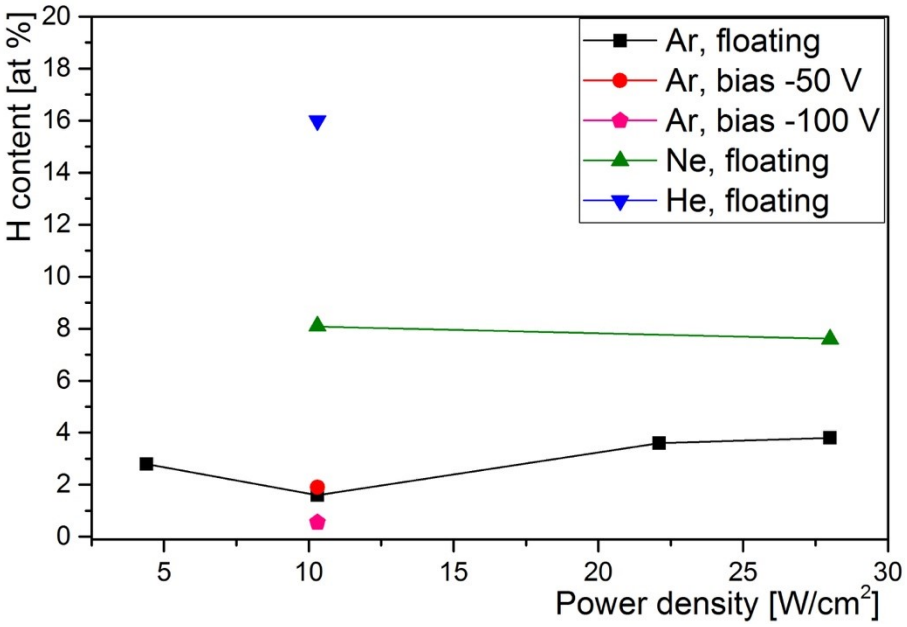

Figure 4.17: H content of a-C films measured with ERDA.

5 Discussion

The most apparent effect of the rising power density, affecting the a-C coating properties is the increase of the substrate temperature. The substrate heating during deposition can be explained by numerous factors:

- The increase of power density leads to heating of the target. The gas then transfers the heat, which results in elevated substrate temperatures (Fig. 4.3) [10,26].

- An increase of the power density leads to a higher energy of the particles bombarding the coating surface, due to an increased voltage at the target, which is especially present for the deposition in Ar (Fig. 4.3 b)). When the target voltage increases, the inert gas ions sputtering the target surface gain a higher energy, and consequently the atoms are sputtered with a higher energy. In addition, neutralized inert gas atoms are reflected at higher energies.

- An elevated target power does not only increase the energy of the particles bombarding the film, but also the number of those particles reaching the substrate surface per time unit[10]. This can be seen from the increase of deposition rate at higher power densities (Fig. 4.5) and results in an increase of condensation energy at the substrate surface.

Furthermore, the substrate heating is influenced by the type of process gas. This can be explained by several factors:

- The significant increase of the substrate temperature of samples deposited in He and Ne atmospheres is due to the fact that their temperature dependent thermal conductivities are higher than that of Ar [48]. While the thermal conductivity of Ar at 300 K and 1 bar is 17.9 mW/m K, the values of Ne and He are 49.8 and 156.7 mW/m K, respectively [49]. Thus, the energy introduced to the target is transferred more easily to the substrate surface and results in higher temperatures.

- The mean free path of Ne and especially He is higher than that of Ar, which also has an effect on the substrate temperature. This is due to the fact that the probability of atoms colliding with each other decreases and therefore they lose less energy on their way from the target to the substrate surface [23,26].

- The condensation heat and the reflection of ions as neutrals from the cathode contribute significantly to the deposition energy [50]. The reflection of the ions is especially relevant for low mass gases, as is the used gas He, where the reflection is large and the sputter yield low [50].

- The kinetic energy of the ions bombarding the substrate surface is increased by accelerating these ions through an applied bias voltage at the substrate. As a result, the substrate temperature increases, which is seen in the case of those films deposited at a bias potential of -50 and -100 V in Ar atmosphere (Fig. 4.4 b)) [51]. Also, the same is apparent for the floating potential of the depositions in Ne and He. Their floating potential lies around -60 and -80 V, resulting in a more pronounced acceleration of the ions and therefore higher substrate temperatures (Fig. 4.4 a)).

The deposition rate presented a stronger rise with increasing power density than a linear trend would indicate (Fig. 4.5). It is reported in literature that an increased deposition rate causes a decrease in mass density [15,16]. This effect could explain the superlinear increase of the deposition rate with power density with the rising substrate temperature at higher discharge powers. The density decreases, thus leading to thicker films with a lower mass density. The increase of the deposition rate in a-C coatings is also often correlated with the enhancement of the sp^2 content, leading to a decrease in coating density [35]. This predominately occurs when the film experiences high local temperatures during the deposition. The effect of the sp^2 bonds on the density of the film, which is a result of the increasing substrate temperature, has also been found for arc-evaporated coatings [35].

The results of the Raman measurements showed that the sp^2 structure is the primary bonding type of all investigated films. The G-peak position, which ranges from 1560 to 1580 cm^{-1} and the I(D)/I(G) ranging from 1.2 to 1.9 (Fig 4.11), attribute the structure of the films to stage two of the stage model proposed by Ferrari and Robertson [21]. In this stage, the shift of the G-peak position to higher wavelengths and the increase of the I(D)/I(G) intensity ratio with increasing substrate temperatures suggest, that the structure of the deposited films resembles nano-crystalline graphite in contrast to sp^2 a-C [21]. At higher power densities, the substrate temperature is the most important factor in determining the structure of the coatings. The surface mobility of the atoms expands with a further increase of substrate temperature, resulting in crystalline film growth and consequently a graphitization of the film [52]. The Raman measurements yielded, that with increasing power the intensity ratio of the D-peak over the G-peak increases. The intensity ratio rises proportionally to the number and clustering of aromatic rings. Consequently, a reduction of the sp^3 phases to less than 10 % follows and the grain size L_a increases to over 2 nm [21]. Graphite possesses a lower density

than diamond, which suggests that the increases of graphitisation at higher substrate temperatures results in a reduction of coating density [1]. The Raman results also support the assumption that the enhanced deposition rate is a result of the decreasing coating density.

The impurity content of the a-C coating has a large effect on its mass density and structure [16]. These impurities are inert gases (Ar, Ne, He), which are trapped in the carbon film and O and H impurities originating from desorption from the deposition chamber surface [23,16]. These gas atoms are incorporated into the growing coating during the deposition process [23]. As reported in literature, and can also be seen from the presented results, their concentration strongly depends on the substrate temperature, the gas pressure and the bias voltage applied to the substrate [16]. The reflected neutralized ions can be imbedded in the coating when their kinetic energy is high enough. However, it is more likely that incoming reflected inert gas ions sputter previously adsorbed atoms than sticking to the surface [16]. When the substrate is heated, the inert gas incorporation of the thin film is therefore reduced, due to desorption before they can be covered by the arriving C atoms [23]. This explains the decrease of the inert gas impurity content with rising power density (Fig. 4.15). The significant rise in the Ar content of the coatings deposited at a negatively charged bias voltage is due to the enhanced kinetic impact energy of the accelerated, positively charged gas ions. As a result, the Ar content in the film increases due to a higher probability of atom incorporation, see Fig. 4.15 [16,17,53]. O and H impurities most probably originate from condensed H_2O in the deposition chamber [15]. The H_2O vapour outgasses from the chamber wall during the deposition and dissociates in the discharge to form H and O atoms. This assumption is corroborated by the fact that the H content in the coatings is approximately twice the O content (Fig. 4.16 and Fig. 4.17). The desorption of H_2O from the chamber increases with rising temperatures and therefore results in a more pronounced incorporation of O and H atoms at higher power densities [23,15].

Electric properties of a-C coatings are controlled by the conductive sp^2 phase, while the hard sp^3 bonds control the mechanical properties [1]. The decreasing hardness and elastic modulus values over power density (Fig. 4.13) can be associated with the increase of the nano-crystalline graphite phase and the reduction of the harder sp^3 phase, as well as the reduction of the density of the coating. Furthermore, the mechanical properties strongly correlate with the residual stress within the film [1]. The higher the residual stress in the film, the higher the elastic modulus and hardness [1]. This is illustrated by the example of the coatings deposited in Ne and in Ar with an applied bias voltage of -100 V, where both, hardness and residual stress are extremely high (Figs. 4.12 and 4.13 (b)). The coating deposited with a bias voltage of -100 V possesses the highest stress value of all coatings, which correlates with the highest hardness and elastic modulus. Internal stresses are usually strongly influenced by the deposition rate and the energy of the deposited particles. When the deposition rate and

the particle energy increases, the thermally activated atom movements on the coating surface decreases, resulting in harder coatings with elevated residual stress [51,17]. However, the coatings deposited in this thesis possessed a constant residual stress over power density. Although the thermal activation decreases with increased deposition rate at higher power density, the temperature increases. Therefore, the stress value is not influenced. However, although the stress remains constant, the hardness decreases versus power density, which is owing to the increasing graphitisation of the film and the accompanied reduction of the sp^3 bonds [1], as mentioned above.

Elevated levels of inert gas impurities cause compressive stresses in the film [16]. The inert gas atoms form substitutional impurities, which results in compressive stresses within the deposited coating. Therefore, it can be concluded that the elevated stress levels are related to the incorporated gas impurities. This explains the higher stress levels of coatings deposited in Ar with an applied bias voltage and coatings deposited in Ne atmosphere. These samples possess the highest inert gas impurity content and also the highest compressive stress. Consequently, their hardness is the highest of all the analysed coatings [16,17]. The decrease of the inert gas content versus deposition temperature and the resulting lower residual stress values are additional factors to the increasing graphitisation, which lowers the hardness of the coatings.

It was found that the substrate temperature did not only influence the mechanical properties, but also significantly affects the electrical resistivity of the coatings. Overall, the electrical resistivity of the films declined with power density (Fig. 4.14). The decrease of the electrical resistivity stems from the rising substrate temperatures accompanied by the favoured nano-crystalline graphite growth [15,16]. The band gap and therefore the resistivity of the coating is reduced by the increased number of sp^2 bonded carbon atoms, while a high amount of sp^3 fraction would widen the band gap and therefore increase the electrical resistivity [7]. Hence, the resistivity decreases with the increased graphitization at higher discharge powers.

6 Summary

The aim of this study was to investigate the effect of the sputter deposition process on carbon coatings grown in different atmospheres. The influence of the deposition gas, the substrate bias and the power density on the deposition and properties of amorphous carbon films during unbalanced magnetron sputtering of a graphite target was investigated. Carbon films with thicknesses between 1.3 and 2.5 µm were deposited in Ar, Ne and He atmospheres, at power densities between 4.4 and 28 W/cm^2. The substrate temperature was found to rise with increasing power density, bias voltage and thermal conductivity of the deposition gas. The microstructure of the films was characterized using both X-ray diffraction and Raman spectroscopy, which revealed that the coatings mainly consisted of nano-crystalline graphite with predominant sp^2 bonding. With rising substrate temperature at elevated power densities, an increase of the graphitic component was found. From cross-section images taken by scanning electron microscopy, the deposition rate of the coatings was found to increase more pronounced with rising power density than a linear trend would indicate. This suggests that the mass density of the coatings decreases with power density, which can be linked to the graphitisation of the film. The chemical composition of the coatings was determined using elastic recoil detection analysis and revealed that the main impurities of the carbon films were O, H and atoms implanted from the working gas. The content of impurities is related to the substrate temperature, bias voltage and type of deposition gas used. The increase in substrate temperature with power density leads to a decrease of the electrical resistivity, elastic modulus and hardness. Coatings grown in Ar at floating potential possessed the highest resistivity, while coatings deposited at higher bias potentials possessed lower resistivity. Films deposited at high bias voltages furthermore shows the highest residual stress values and consequently the highest hardness, which could be correlated to the high working gas content incorporated with increasing bias. The residual stresses for these coatings ranged from -300 to -2900 MPa and respective hardness values of 10 to 33 GPa were obtained. In conclusion it was found, that the substrate temperature and the impurity content are the most influential factors determining the microstructure and the mechanical and electrical properties of the amorphous carbon films.

7 Literature References

[1] J. Robertson, Diamond-like amorphous carbon, Mater. Sci. Eng. R Reports 37 (2002) 129–281.

[2] T.D. Burchell, Carbon Materials for Advanced Technologies, Pergamon, Oxford, 1999.

[3] M.H. Nazare, A.J. Neves, Properties, Growth and Applications of Diamond, The Institution of Electrical Engineers, London, 2001.

[4] H.O. Pierson, Handbook of Carbon, Graphite, Diamond and Fullerenes, Noyes Publications, Park Ridge, 1993.

[5] P. Sllva, S. Ravi, Properties of amorphous carbon, The Institution of Electrical Engineers, London, 2003.

[6] A. Erdemir, C. Donnet, Tribology of diamond-like carbon films, J. Appl. Phys. 39 (2006) 311–327.

[7] N. Cho, K.M. Krishnan, D.K. Veirs, M.D. Rubin, C.B. Hopper, B. Bhushan, Chemical structure and physical properties of diamond-like amorphous carbon films prepared by magnetron sputtering, J. Mater. Res. 5 (1990) 2543–2554.

[8] C. Donnet, A. Erdemir, Tribology of Diamond-Like Carbon Films, Springer, New York, 2008.

[9] V. Tiainen, Amorphous carbon as a bio-mechanical coating — mechanical properties and biological applications, Diam. Relat. Mater. 10 (2001) 153–160.

[10] A.A. Onoprienko, V. V. Artamonov, I.B. Yanchuk, Effect of magnetron discharge power on the resistivity and microstructure of carbon films, Surf. Coat Tech. 200 (2006) 4174–4178.

[11] D.R. McKenzie, Tetrahedral bonding in amorphous carbon, Rep. Prog. Phys. 59 (1996) 1611–1664.

[12] S. Aisenberg, R. Chabot, Ion-beam deposition of thin films of diamondlike carbon, J. Appl. Phys. 42 (1971) 2953–2958.

[13] G.M. Pharr, D.L. Callahan, S.D. McAdams, T.Y. Tsui, S. Anders, A. Anders, J.W. Ager, I.G. Brown, C.S. Bhatia, S.R.P. Silva, J. Robertson, Hardness, elastic modulus, and structure of very hard carbon films produced by cathodic-arc deposition with substrate pulse biasing, Appl. Phys. Lett. 68 (1996) 779–781.

[14] Y. Liou, A. Inspektor, R. Weiner, R. Messier, The effect of oxygen in diamond deposition by micowave plasma enhanced chemical vapour deposition, J. Mater. Res. 5 (1990) 2305–2312.

[15] E. Mounier, F. Bertin, M. Adamik, Y. Pauleau, P.B. Barna, Effect of the substrate temperature on the physical characteristics of amorphous carbon films deposited by

d.c. magnetron sputtering, Diam. Relat. Mater. 5 (1996) 1509–1515.

[16] C.C. Fang, F. Jones, V. Prasad, Effect of gas impurity and ion bombardment on stresses in sputter-deposited thin films: A molecular-dynamics approach, J. Appl. Phys. 74 (1993) 4472–4482.

[17] E. Mounier, Y. Pauleau, Mechanisms of intrinsic stress generation in amorphous carbon thin films prepered by magnetron sputtering, Diam. Relat. Marerials. 6 (1997) 1182–1191.

[18] M.S. Dresselhaus, G. Dresselhaus, P.C. Eklund, Science of Fullerenes and Carbon Nanotubes, Academic Press, San Diego, 1995.

[19] J. Robertson, Amorphous carbon, Adv. Phys. 35 (1986) 317–374.

[20] W. Jacob, W. Möller, W. Jacob, W. Muller, On the structure of thin hydrocarbon films, Am. Inst. Phys. 63 (1993) 1771–1773.

[21] A. Ferrari, J. Robertson, Interpretation of Raman spectra of disordered and amorphous carbon, Phys. Rev. B. 61 (2000) 95–107.

[22] O. Jantschner, Enhancement of the thermal stability of sputtered diamond-like carbon thin films for automotive applications, University of Leoben, 2014.

[23] D.M. Mattox, Handbook of Physical Vapor Deposition (PVD) Processing, Noyes Publications, Westwood, 1998.

[24] P. Sigmund, Theory of sputtering. I. sputtering yield of amorphpus and Polycrystalline targets, Phys. Rev. 184 (1969) 383–415.

[25] P. Sigmund, Mechanisms and theory of physical sputtering by particle impact, Nucl. Instruments Methods Phys. Res. 27 (1987) 1–20.

[26] R.A. Haefer, Oberflächen und Dünnschicht-Technologie: Beschichtung von Oberflächen, Springer Verlag, Berlin, 1987.

[27] P.J. Kelly, R.D. Arnell, Magnetron sputtering: a review of recent developments and applications, Vacuum. 56 (2000) 159–172.

[28] W.D. Westwood, Sputter Deposition, AVS, New York, 2003.

[29] W.D. Sproul, S. Films, N. Street, S. Barbara, High-rate reactive DC magnetron sputtering of oxide and nitride superlattice coatings, Vacuum. 51 (1998) 641–646.

[30] L.I. Maissel, P.M. Schaible, Thin films deposited by bias sputtering, J. Appl. Phys. 36 (1965) 237–242.

[31] P.J. Fallon, V.S. Veerasamy, C.A. Davis, J. Robertson, G.A.J. Amaratunga, W.I. Milne, J. Koskinen, Properties of filtered-ion-beam-deposited diamondlike carbon as a function of ion energy, Phys. Rev. B. 48 (1993) 4777–4782.

[32] J.J. Cuomo, J.P. Doyle, J. Bruley, J.C. Liu, Sputter deposition of dense diamond-like carbon films at low temperature, Appl. Phys. Lett. 58 (1991) 466–468.

[33] J. Schwan, S. Ulrich, H. Roth, H. Ehrhardt, S. Silva, J. Robertson, R. Samlenski, R. Brenn, Tetrahedral amorphous carbon films prepared by magnetron sputtering and dc ion plating, J. Appl. Phys. 79 (1996) 1616–1422.

[34] H. Hofsäss, H. Feldermann, R. Merk, M. Sebastian, C. Ronning, Cylindrical spike model for the formation of diamondlike thin films by ion deposition, Appl. Phys. A. 66 (1998) 153–181.

[35] M. Chhowalla, J. Robertson, C.W. Chen, S.R.P. Silva, C. a. Davis, G. a. J. Amaratunga, W.I. Milne, Influence of ion energy and substrate temperature on the optical and electronic properties of tetrahedral amorphous carbon (ta-C) films, J. Appl. Phys. 81 (1997) 139–145.

[36] L.G. Jacobsohn, F.L.F. Jr, F.L. Freire, Influence of the plasma pressure on the microstructure and on the optical and mechanical properties of amorphous carbon films deposited by direct current magnetron sputtering influence of the plasma pressure on the microstructure and on the optical and me, J. Vac. Sci. Technol. A. 17 (1999) 2841–2849.

[37] H. Lüth, Solid Surfaces, Interfaces and Thin Films, 4th ed., Springer, Berlin, 2001.

[38] B. Schrader, Infrared and Raman Spectroscopy, VCH, Weinheim, 1995.

[39] R. Singh, C . V . Raman and the Discovery of the Raman Effect, 2002.

[40] R.L. McCreery, Raman Spectroscopy for Chemical Analysis, Wiley-Interscience, New York, 2000.

[41] F. Tuinstra, J.L. Koenig, Raman spectrum of graphite Raman spectrum of graphite, J. Chem. Phys. 53 (1970) 1126–1130.

[42] W. Assmann, H. Huber, C. Steinhausen, M. Dobler, H. Gliickler, A. Weidinger, Elastic recoil detection analysis with heavy ions, Nucl. Instruments Methods Phys. Res. 89 (1994) 131–139.

[43] W.M. Arnold, F.H.P.M. Habraken, Elastic recoil detection, Rep. Prog. Phys. 56 (1993) 859–902.

[44] J. Tirira, P. Trocellier, Elastic recoil detection analysis; theoretical analysis of scattering cross section and basic parameters, J. Radioanal. Nucl. Chem. 130 (1989) 311–319.

[45] D. Winkler, Konzeption und Realisierung eines thermisch unterstützten Messverfahrens zur Bestimmung von Eigenspannungen in dünnen Schichten, University of Leoben, 1997.

[46] G.C.A.M. Janssen, M.M. Abdalla, F. van Keulen, B.R. Pujada, B. van Venrooy, Celebrating the 100th anniversary of the Stoney equation for film stress: Developments from polycrystalline steel strips to single crystal silicon wafers, Thin Solid Films. 517 (2009)

1858–1867.

[47] W.C. Oliver, G.M. Pharr, An improved technique for determining hardness and elastic modulus using load and displacement sensing indentation experiments, J. Mater. Res. 7 (1992) 1564–1583.

[48] I. Petrov, I. Ivanov, V. Orlinov, Comparison of magnetron sputter deposition conditions in neon, argon, krypton, and xenon discharges, J. Vac. Sci. Technol. A. 11 (1993) 2733–2741.

[49] Engeneers edge, Thermal conductivity of gases, http://www.engineersedge.com/heat_transfer/thermal-conductivity-gases.htm, June 2017

[50] S.M. Rossnagel, J.J. Cuomo, W.D. Westwood, Handbook of Plasma Processing Technology, Noyes Publications, Park Ridge, 1990.

[51] M. Ohring, Materials Science Of Thin Films Deposition and Structure, 2nd ed., Academic Press, San Diego, 2002.

[52] Y. Lifshitz, Hydrogen-free amorphous carbon films: correlation between growth conditions and properties, Diam. Relat. Mater. 5 (1996) 388–400.

[53] J.J. Cuomo, R.J. Gambio, Incorporation of rare gases in sputtered amorphous metal films, J. Vac. Sci. Technol. 14 (1977) 152–157.